J. Fluid Mech. (2024), *vol*. 986, A36, doi:10.1017/jfm.2024.348

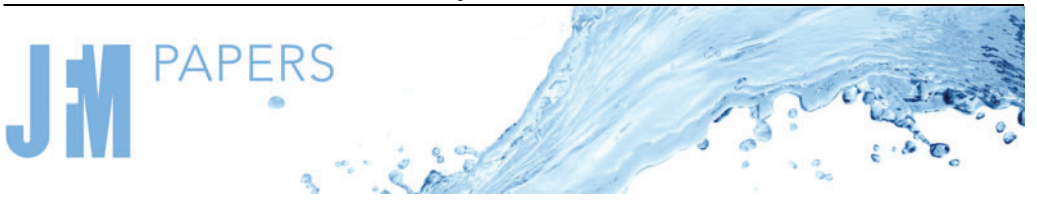

Small-scale turbulent characteristics in transcritical wall-bounded flows

Fangbo Li[1],†, **Weiwei Zhang**[1], **Bofeng Bai**[2] **and Matthias Ihme**[3,4],†

[1]School of Aeronautics, Northwestern Polytechnical University, Xi'an, Shaanxi 710072, China

[2]School of Energy and Power Engineering, Xi'an Jiaotong University, Xi'an, Shaanxi 710049, China

[3]Department of Mechanical Engineering, Stanford University, Stanford, CA 94305, USA

[4]Department of Photon Science, SLAC National Accelerator Laboratory, Menlo Park, CA 94025, USA

(Received 16 July 2023; revised 1 March 2024; accepted 1 April 2024)

Considerable efforts have been devoted to the understanding of the small-scale characteristics in turbulent flows. While the universality of small-scale quantities has been established for incompressible flows, their extension to high-pressure transcritical flows remains an open area of research. To address this question, we investigate the real-fluid thermodynamic effects on small-scale velocity statistics of high-pressure transcritical wall-bounded turbulence. We show that in the locally isotropic region for transcritical flows, low-order moments of small-scale statistics collapse for all cases and Kolmogorov's (1941) theory holds. However, real-fluid thermodynamic effects introduce deviations in the tails of the probability density function for the velocity derivative and, consequently, high-order moments of velocity gradients and dissipation rate in transcritical flows cannot collapse in the locally isotropic region. Analysis of the intermittency shows that the low-order structure functions in transcritical flows follow extended self-similarity, while the dependence of the intermittency factor on real-fluid effects is observed for high-order structure functions. The real-fluid effects on intermittency are explained by turbulent structures related to rare events. Additionally, the dissipation rate moments for transcritical flows follow a universal scaling with Reynolds number, and the scaling exponents are different from those of incompressible flows. These results extend the small-scale universality in incompressible flows (Schumacher *et al.*, *Proc. Natl Acad. Sci. USA*, vol. 111, 2014, pp. 10961–10965) to realistic flows with significant changes in thermodynamic properties, and provide a physical underpinning of the scaling laws of small-scale statistics at transcritical conditions.

Key words: turbulence simulation, turbulent boundary layers

† Email addresses for correspondence: fbli@nwpu.edu.cn, mihme@stanford.edu

1. Introduction

Investigating the turbulent small-scale properties that are related to the dissipative scale in the energy cascade, such as velocity gradients, dissipation rate and dissipation scale, is of great interest to both the engineering and environmental communities. These quantities play an important role in turbulence modelling by providing the foundation for modelling subgrid stresses and closures for the transport equation of the dissipation rate (Antonia, Kim & Browne 1991; Sreenivasan & Antonia 1997). The standard paradigm of small-scale universality proposed by Kolmogorov (1941) is that while the large-scale turbulent motions are non-universal, an increasing degree of universality is imparted to small scales with increasing separation between the large and small scales.

Local isotropy was introduced by Kolmogorov (1941) to describe the universality of the small scales of turbulent motions. This paradigm is a cornerstone of universal self-similarity, which assumes complete independence of the small-scale structure from large-scale structures (Kolmogorov 1941; Mestayer 1982). Since Kolmogorov postulated the universality of small scales, many experiments and direct numerical simulations (DNS) of incompressible turbulence have verified the universal small-scale properties for locally isotropic incompressible flows. Hamlington *et al.* (2012) performed DNS of incompressible channel flows with friction Reynolds number $Re_\tau = 180$, 381 and 590, and found that in the locally isotropic region, the local dissipation scale and dissipation-rate moments behave similarly to those of isotropic flows. Djenidi *et al.* (2017) found that in the locally isotropic region of incompressible wall-bounded flows, the moments of small-scale statistics for wall-bounded flows, such as the skewness (S) and flatness (F) of velocity gradients, remain approximately constant with increasing wall distance ζ^+ and Taylor Reynolds number Re_λ, where $Re_\lambda = \rho u_{rms}\lambda/\mu$ with λ the Taylor microscale, ρ the density, μ the dynamic viscosity, $\lambda = u_{rms}/\overline{(\partial u'/\partial x)^2}^{1/2}$ and $u_{rms} = \sqrt{\overline{u'^2}}$ (Djenidi *et al.* 2017), *viz.*

$$S_{\partial u'/\partial x} = \frac{\overline{(\partial u'/\partial x)^3}}{\overline{(\partial u'/\partial x)^2}^{3/2}} = \text{const.}, \quad F_{\partial u'/\partial x} = \frac{\overline{(\partial u'/\partial x)^4}}{\overline{(\partial u'/\partial x)^2}^2} = \text{const.}, \tag{1.1a,b}$$

with u' and x denoting the streamwise velocity fluctuation and streamwise coordinate, respectively. These findings indicate that in the locally isotropic region of incompressible wall-bounded flows, the turbulent small-scale quantities in all cases exhibit universal behaviour, which is independent of Reynolds number and ζ^+. By studying homogeneously isotropic turbulence, turbulent shear flows and thermal convection, Schumacher *et al.* (2014) showed that probability density functions (PDFs) of velocity gradients and moments of dissipation obey the universality of small scales for different flows even at moderate Reynolds numbers. Furthermore, Boschung *et al.* (2016) examined structure functions in the dissipative range, and reported Reynolds-number-independent structure function and universal scaling for local-dissipation-rate moments for incompressible, locally isotropic flows. Schumacher (2001) reported increasing derivative moments of streamwise velocity with Re_λ for orders $n > 4$ in incompressible, homogeneous shear flows. Similar results for small-scale statistics of incompressible flows were reported by Kim & Antonia (1993), Sreenivasan & Antonia (1997), Antonia *et al.* (2015) and Elsing & Marusic (2010). With regard to compressible flows with high Mach number, Huang, Coleman & Bradshaw (1995) showed that the dissipation rate induced by the dilatation and viscous fluctuations is very small, implying the similarity of turbulent dissipation between compressible and incompressible flows.

Transcritical wall-bounded turbulence at supercritical pressure conditions with intense density fluctuations are encountered in many technical applications. The thermodynamic properties of fluids at supercritical pressures differ from those at subcritical conditions. In particular, at supercritical pressures, the transitioning from the liquid-like phase to gas-like phase as the temperature increases, which is called 'transcritical conditions', can occur without the formation of the interface (Simeoni *et al.* 2010; Bolmatov, Brazhkin & Trachenko 2013; Simeski & Ihme 2023). Thermodynamic and transport properties, including density, viscosity, specific heat capacity and thermal conductivity, vary significantly across the Widom line as the increasing temperature, thereby introducing significant real-fluid thermodynamic effects (Simeoni *et al.* 2010; Bolmatov *et al*. 2013; Ma, Yang & Ihme 2018; Guo, Yang & Ihme 2022; Li *et al.* 2023). It has been confirmed that real-fluid thermodynamic effects which are induced by strong variations in thermal properties considerably change the large-scale structures of wall-bounded turbulence (Patel *et al.* 2015; Ma *et al.* 2018; Kawai 2019; Kim, Hickey & Scalo 2019; Guo *et al.* 2022; Li *et al.* 2023). Sciacovelli, Cinnella & Grasso (2017) carried out systematic DNS investigations to study small-scale structures of isotropic turbulence of high-pressure dense fluids which have similar physical properties to transcritical fluids, their analysis showed a weakening of compressive structures and an enhancement of expanding ones. They reported that the dense gas temperature variations are negligible due to the decoupling of dynamic and thermal effects, and the fluid viscosity exhibits a smaller root-mean square (r.m.s.) than perfect gas, suggesting the structures considered in their work are mainly related to the genuine compressibility and shocklet. Furthermore, the dissipation rate of transcritical flows, which is dominated by the dissipative range, behaves quite similarly to that of high-Ma compressible flows, with the fluctuating thermal properties contributing insignificantly to the dissipation rate (Li *et al.* 2023). These raise some important questions to be addressed. Will real-fluid effects invalidate the universality of the small-scale dynamics? What are the effects of variable thermodynamic properties on the small-scale dynamics? Current efforts have not yet provided evidence for the universality of small-scale statistics at transcritical conditions with strong variations of thermal properties. To the best of our knowledge, there has been no prior discussion about turbulent small-scale characteristics at high-pressure transcritical conditions in the scientific literature. A study utilizing high-resolution DNS data in an effort to examine the small-scale universality at transcritical conditions can therefore provide the theoretical framework for developing scaling laws and turbulence models to improve their accuracy and generalization.

To address these issues, the present work examines the statistics related to the small-scale properties in transcritical channel flows utilizing DNS data. The Re_τ currently considered in this study ranges between 300 and 1370. As in Hamlington *et al.* (2012), Schumacher *et al.* (2014) and Djenidi *et al.* (2017) for incompressible flows, we focus on the moments of the velocity gradients and the dissipation rate, to investigate the scalings for statistics associated with the small-scale properties. The main objective of this study is to examine the hypothesis of the consistency of these small-scale quantities between transcritical and incompressible flows, and to interpret the modulations on the turbulent statistics and intermittency related to the small-scale properties by variable thermodynamic property arising from real-fluid conditions.

The remainder of this paper is organized as follows. Section 2 presents our DNS database, which includes details of the overall computational set-up and cases. Section 3 presents results and the associated interpretations. Finally, § 4 offers conclusions.

Cases	$T_{r,hot}$	$T_{r,cold}$	$\rho_{r,hot}$	$\rho_{r,cold}$	$Re_{\tau,hot}$	$Re_{\tau,cold}$	Density ratio ($\rho_{w,cold}/\rho_{w,hot}$)
TR3	2.38	0.79	0.12	2.17	300	430	17.8
TR1.9	1.51	0.79	0.22	2.17	610	440	10.1
TR1.4	1.11	0.79	0.42	2.17	1370	500	5.2
TR1	0.79	0.79	2.17	2.17	700	700	1

Table 1. Summary of cases and conditions, with the subscripts hot and cold indicating the values at the hot wall and the cold wall. Here, $p_r = p/p_c$, $T_r = T/T_c$, $\rho_r = \rho/\rho_c$ are reduced pressure, temperature and density, respectively.

2. Direct numerical simulations

2.1. *Problem formulation*

The database used for the present analysis was obtained from DNS of a straight turbulent channel of transcritical nitrogen (Ma *et al*. 2018; Guo *et al*. 2022; Li *et al.* 2023). For the broader use of the transcritical DNS database by the turbulence and combustion community, we have made this database open-access on https://blastnet.github.io/index.html (Chung *et al.* 2022). The flow has a reduced bulk pressure (defined as $p_r = p/p_c$ with p_c the critical pressure) of 1.14, with the temperatures for the hot wall and the cold wall kept spatially and temporally constant. The size of the flow domain is L_x (streamwise, x) $\times$ $2L_y$ (wall normal, y) $\times$ L_z (spanwise, z), with $L_x/L_y = 2\pi$, $L_z/L_y = 4\pi/3$, and the channel height measuring $2L_y = 9 \times 10^{-5}$ m. The spatial coordinate is defined over $0 \le x \le L_x$, $-L_y \le y \le L_y$ and $0 \le z \le L_z$. We use ζ to denote the wall distance.

The fully conservative, compressible continuity, momentum and total energy equations are solved. The Peng–Robinson (PR) equation of state (EoS) (Peng & Robinson 1976) and Chung's transport-property model (Chung *et al.* 1988) are employed to describe the thermodynamics of the working fluid. These models have been used in past DNS studies on turbulence of transcritical fluids (Miller, Harstad & Bellan 2001; Ma *et al*. 2018; Kim *et al*. 2019; Toki, Teramoto & Okamoto 2020; Guo *et al*. 2022; Li *et al.* 2023). In Appendix A, we discuss the EoS and the transport-property model in more detail. Further information of the DNS configurations, numerical methodology and validations can be found in Ma *et al*. (2018) and Guo *et al*. (2022). As summarized in table 1, the current database is composed of four transcritical cases, TR3, TR1.9, TR1.4 and TR1 (where TR denotes the temperature ratio between the hot wall and the cold wall) with a reduced temperature of $T_{r,cold} = T/T_c = 0.79$ at the cold wall. These conditions are selected to examine the real-fluid effects induced by thermal property changes under substantial heat transfer conditions on the small-scale turbulent statistics. For all cases, the Mach number is less than 0.16, indicating that the configurations in all cases correspond to the low-speed flow regime. Across the majority of the channel, the spatial resolution is $\Delta x = (2.4 \sim 4)\bar{\eta}$, $\Delta y = (0.4 \sim 3.2)\bar{\eta}$, $\Delta z = (1.6 \sim 3)\bar{\eta}$ with $\bar{\eta}$ being the mean Kolmogorov length scale, $\bar{\eta} = [(\bar{\mu}/\bar{\rho})^3 \bar{\rho}/\bar{\varepsilon}]^{1/4}$, where μ is the dynamic viscosity, ρ is the density and ε is the dissipation rate of turbulent kinetic energy, $\varepsilon = \tau'_{ij}(\partial u'_i/\partial x_j)$ and τ_{ij} the viscous stress tensor. Expressed in wall units, these conditions correspond to $\Delta x^+ = 4.9 \sim 8$, $\Delta z^+ = 3.26 \sim 6.8$, $\Delta y^+ = 0.29 \sim 0.47$ at the cold wall and $\Delta y^+ = 0.2 \sim 1$ at the hot wall.

2.2. *Cases set-up and grid resolutions*

Seeking the statistically accurate small-scale velocity moments requires finer resolutions and longer integration time, here we briefly review the typical resolutions in the literatures that considered velocity-derivative skewness, flatness and high-order moments. van de Water & Herweijer (1999) measured the high-order structure functions for incompressible turbulence (with the order n up to 20), characteristic parameters of their isotropic flows are $Re_\lambda < 810$ with the spatial resolution evaluated by l_p/η (l_p is the probe length) being $l_p/\eta \approx 2$. The scaling exponents of nth order passive scalar structure functions ($n \leq 8$) in incompressible flows were examined by Lepore & Mydlarski (2012), Re_λ considered in their study was 370 with the spatial resolution being $\Delta x = 3.25\eta$. Schumacher (2001) carried out DNS investigations of incompressible homogeneous shear flows with Re_λ from 59 up to 99 to compare the high-order small-scale statistics ($n < 8$), the grid spacing in the y-direction is $\Delta y = (0.5 \sim 1.6)\eta$. Pumir, Xu & Siggia (2016) used DNS to calculate high-order moments of velocity gradients in the incompressible channel flow at $Re_\tau \approx 1000$, the gird in wall units is $\Delta x^+ = \Delta z^+ = 15.7$. In the DNS examinations on local dissipation scale and high-order dissipation moments of incompressible channel flows conducted by Hamlington *et al.* (2012), Re_τ of their cases is 180, 381 and 590 with the resolution $\Delta x^+ = 1.8 \sim 4.4$, $\Delta y^+_{max} = 0.55 \sim 0.91$, $\Delta z^+ = 1.8 \sim 2.2$. Analysis of small-scale dynamics for compressible isotropic flows was conducted by Sciacovelli *et al.* (2017), using a grid spacing of $\Delta x \approx 2.3\eta$. Hence, the resolutions in the present work are comparable to those employed in prior studies on turbulent velocity gradients, dissipation rate and their moments (van de Water & Herweijer 1999; Schumacher 2001; Hamlington *et al.* 2012; Lepore & Mydlarski 2012; Pumir *et al.* 2016). Further evidence to examine the small-scale grid convergency and ensure that the dissipative scale is sufficiently resolved can be found in Appendix B. To obtain converged results for statistical moments, we average over homogeneous directions and time using data in 20 flow-through times, where one flow-through time is defined as $L_x/\overline{u_b}$, with $\overline{u_b}$ being the bulk velocity.

2.3. *Overview of the fluctuating thermodynamic properties*

Figure 1 shows the plots for r.m.s. quantities of thermodynamic and transport properties (i.e. density, constant-pressure specific heat capacity, dynamic viscosity and thermal conductivity) in the present transcritical cases. Significant fluctuations of thermodynamic and transport properties can be found, especially near the hot wall. The density fluctuations (i.e. ρ_{rms}) reach 40 % of the mean value (figure 2*a*), while $c_{p,rms}$ is most significant and its maximum exceeds 100 % of the mean value (figure 2*b*). The fluctuations of transport properties (i.e. μ_{rms} and λ_{rms}) also reach 30 % of the mean value (figure 2*c*,*d*). To address the influences of the real-fluid thermodynamic effects on transcritical turbulence, here we compare the thermal-property fluctuations with those in the previous studies on compressible flows. For supersonic turbulent boundary layers, ρ_{rms} is small compared with $\bar{\rho}$ (Bradshaw 1977), which is known as Morkovin's hypothesis. Generally, $\rho_{rms}/\bar{\rho}$ in supersonic compressible flows does not exceed 10 % (Coleman, Kim & Moser 1995; Huang *et al.* 1995; Zhang *et al.* 2012, 2022). However, the density fluctuations $\rho_{rms}/\bar{\rho}$ in the present transcritical cases exceed the level of hypersonic flows for ideal gas with Mach number $Ma = 11.93$ (Duan, Beekman & Martin 2011), indicating that compressibility induced by real-fluid thermodynamic effects is significant to change turbulent structures. As shown in figure 2(*b–d*), for transcritical cases, c_p and transport properties also exhibit very large fluctuations (the r.m.s. in c_p is most significant and even reaches the mean value), which can definitely result in noticeable impacts on momentum and scalar

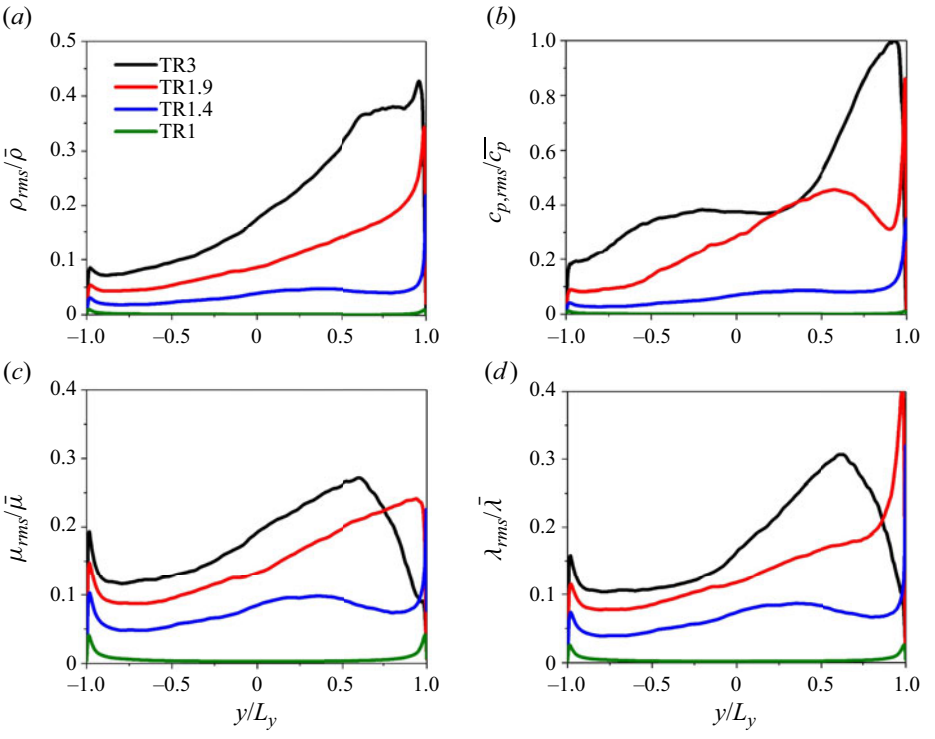

Figure 1. Plots for r.m.s. quantities of thermodynamic and transport properties for all cases: (*a*) ρ; (*b*) c_p; (*c*) dynamic viscosity μ; (*d*) thermal conductivity λ. All results of the r.m.s. quantities are normalized by the Reynolds-averaged mean quantities.

statistics. In contrast, supersonic flows generally use the thermal-property models for ideal gas, thus the fluctuations of c_p, μ and λ are quite weak and influence turbulence dynamics negligibly. In summary, the real-fluid thermodynamic effects at high-pressure transcritical conditions induce appreciable fluctuations of thermodynamic and transport properties, Morkovin's hypothesis is invalid and the resultant turbulent dynamics may deviate significantly from incompressible flows and supersonic flows.

We note that for all cases, the Mach number is less than 0.16, indicating that the configurations in all cases correspond to the low-speed flow regime. Moreover, the pressure change in the channels is very small (the instantaneous p/p_c changes by less than 0.5 % within the whole channel). Hence the dominant effects in the transcritical cases are the significantly variable properties induced by the temperature variations present at low Mach numbers.

3. Results and discussions

In this section we begin showing the small-scale quantities and examine the effects of variable thermodynamic properties at real-fluid conditions on these statistics using the established transcritical DNS database. For the following discussions, the Reynolds average for a variable Z is denoted as $\bar{Z}$ and the Favre average is denoted by $\tilde{Z} = \overline{\rho Z}/\bar{\rho}$. Their fluctuations are defined as Z' and Z'', respectively.

3.1. *Examinations of local isotropy*

Near the wall, the flow is highly anisotropic due to wall effects, the flow quantities are sensitive to the boundary conditions and thus the universality of small-scale quantities can hardly be observed. Therefore, examining the results in the locally isotropic region is effective for evaluating the universality of statistics in the presence of the real-fluid effects since the wall effects have been largely eliminated. We begin with examining the validity of local isotropy of small-scale statistics. Provided that the flow is locally isotropic, the even moments of velocity gradient should obey the following relations (Taylor 1935; Jiang *et al.* 2022):

$$\overline{\left(\frac{\partial u'}{\partial x}\right)^2} = \overline{\left(\frac{\partial v'}{\partial y}\right)^2} = \overline{\left(\frac{\partial w'}{\partial z}\right)^2} = \frac{1}{2}\overline{\left(\frac{\partial u_i'}{\partial x_j}\right)^2}, \tag{3.1}$$

with $i \neq j$ and no summation on i and j. Thus, the local isotropy of the second-order moments of velocity gradients indicates

$$A_1 = \overline{\left(\frac{\partial u'}{\partial x}\right)^2} \Big/ \overline{\left(\frac{\partial v'}{\partial y}\right)^2} = 1, \quad A_2 = \overline{\left(\frac{\partial u'}{\partial x}\right)^2} \Big/ \overline{\left(\frac{\partial w'}{\partial z}\right)^2} = 1, \tag{3.2a}$$

$$A_3 = 2\overline{\left(\frac{\partial u'}{\partial x}\right)^2} \Big/ \overline{\left(\frac{\partial u'}{\partial y}\right)^2} = 1, \quad A_4 = 2\overline{\left(\frac{\partial u'}{\partial x}\right)^2} \Big/ \overline{\left(\frac{\partial u'}{\partial z}\right)^2} = 1, \tag{3.2b}$$

$$A_5 = 2\overline{\left(\frac{\partial u'}{\partial x}\right)^2} \Big/ \overline{\left(\frac{\partial v'}{\partial x}\right)^2} = 1, \quad A_6 = 2\overline{\left(\frac{\partial u'}{\partial x}\right)^2} \Big/ \overline{\left(\frac{\partial v'}{\partial z}\right)^2} = 1, \tag{3.2c}$$

$$A_7 = 2\overline{\left(\frac{\partial u'}{\partial x}\right)^2} \Big/ \overline{\left(\frac{\partial w'}{\partial x}\right)^2} = 1, \quad A_8 = 2\overline{\left(\frac{\partial u'}{\partial x}\right)^2} \Big/ \overline{\left(\frac{\partial w'}{\partial y}\right)^2} = 1. \tag{3.2d}$$

According to Tang *et al.* (2015), the local isotropy of the third-order and fourth-order moments of the velocity gradient leads to

$$S_{\partial u'/\partial x} = S_{\partial v'/\partial y} = S_{\partial w'/\partial z}, \tag{3.3}$$

$$F_{\partial u'/\partial x} = F_{\partial v'/\partial y} = F_{\partial w'/\partial z}. \tag{3.4}$$

Figure 2 examines the local isotropy of the small-scale statistics along the wall-normal direction. In figure 2(*a*), we show the Lumley triangle, which examines the non-zero invariants I_1 and I_2 of the anisotropic part of the Reynolds stress tensor $a_{ij} = \overline{u_i'u_j'}/\overline{u_k'u_k'} - \delta_{ij}/3$, with $I_1 = \sqrt{a_{ij}a_{ji}/6}$ and $I_2 = (1/6a_{ij}a_{jk}a_{ki})^{1/3}$. As in Lumley & Newman (1977), the triangle corresponds to $I_1 = I_2$, $I_1 = -I_2$ and $I_1 = \sqrt{2I_2^3 + 1/27}$. As the distance to the wall increases, the variants approach $I_1 = 0$ and $I_2 = 0$ which corresponds to the isotropic condition, as indicated by the arrow, implying that the departure from isotropy becomes smaller. Figure 2(*b*) shows the wall-normal distribution of A_i for TR3. The results confirm that at $0.3 < \zeta/L_y < 1$ near both walls, A_i shows a gradual convergence towards unity and lies within the $\pm 20\,\%$ boundaries of local isotropy (indicated by the dashed lines), which suggests that the local isotropy hypothesis within this wall-normal range ($0.3 < \zeta/L_y < 1$) is approximately valid. The results for other cases are similar to those of TR3 and are not shown here for brevity. Figure 2(*c*) shows the skewness of the velocity gradient components according to (3.3). It can be seen that at $\zeta/L_y > 0.25$ near both walls, all distributions exhibit a region where the magnitudes of the velocity-derivative skewness

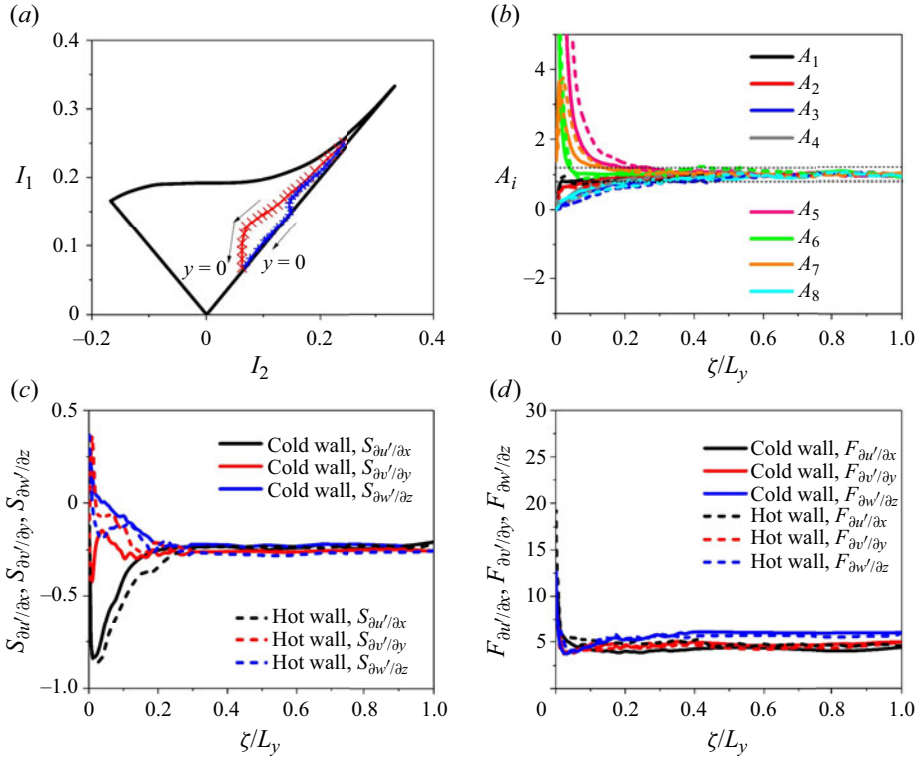

Figure 2. Examinations of the local isotropy along the wall-normal direction for TR3: (*a*) the turbulence-invariant map which shows I_1 as a function of I_2 for the anisotropic tensor of Reynolds stress a_{ij} near the hot wall (red line and symbols) and the cold wall (blue line and symbols); (*b*) verification of local isotropy of second order moments by examining A_i from (3.2), with the dashed lines denoting the $\pm 20\,\%$ boundaries of local isotropy ($A_i = 1$); (*c*) verification of local isotropy of third-order moments (see (3.3)); (*d*) verification of local isotropy of fourth-order moments (see (3.4)).

are approximately consistent. Figure 2(*d*) compares the distributions of $F_{\partial u'/\partial x}$, $F_{\partial v'/\partial y}$ and $F_{\partial w'/\partial z}$, showing that the local isotropy condition (3.4) is satisfied reasonably well when $\zeta/L_y > 0.3$. Thus, we can determine the ζ/L_y range of locally isotropic region as $0.3 < \zeta/L_y < 1$ near both walls. According to this, table 2 shows ζ/L_y, ζ^+ and ζ^* of the start point of the locally isotropic region (LIR) of the channel for all cases.

3.2. *Small-scale universality: velocity gradients and dissipation rate*

Figure 3 shows PDFs of the longitudinal two-point velocity increments $\Delta u' = u'(x + r, y, z) - u'(x, y, z)$ at different wall-normal positions for all cases. We find that the PDFs of the longitudinal velocity increments pass through a transition from super-Gaussian to nearly Gaussian (or slightly sub-Gaussian) behaviour as the two-point distance increases (see figure 3*a–d*), suggesting intermittency at the small scales. In figure 3(*a*), it can be seen that all PDF profiles are quite consistent; although the PDFs are close to exponential decay, there are still slight discrepancies among all cases at the tail of the PDF profiles. In the following section, we will address the significance of these tails on the high-order moments of velocity gradients. In the near-wall layer (as shown in figure 3*b*), the discrepancies between different cases are more obvious, which is attributed to the anisotropic nature of the flow near the wall.

Cases	Start point of the locally isotropic region		
	ζ/L_y	ζ^+	ζ^*
TR3 cold wall	0.3	107	268
TR3 hot wall		72	192
TR1.9 cold wall		101	209
TR1.9 hot wall		92	191
TR1.4 cold wall		122	202
TR1.4 hot wall		348	203
TR1		177	212

Table 2. Here, ζ/L_y, ζ^+ and ζ^* of the start point of the locally isotropic region for all cases, where $\zeta^+ = \sqrt{\rho_w \tau_w}\zeta/\mu_w$ and $\zeta^* = \sqrt{\bar{\rho}\tau_w}\zeta/\bar{\mu}$ are wall units and semilocal wall units, respectively, and τ_w is the wall shear stress.

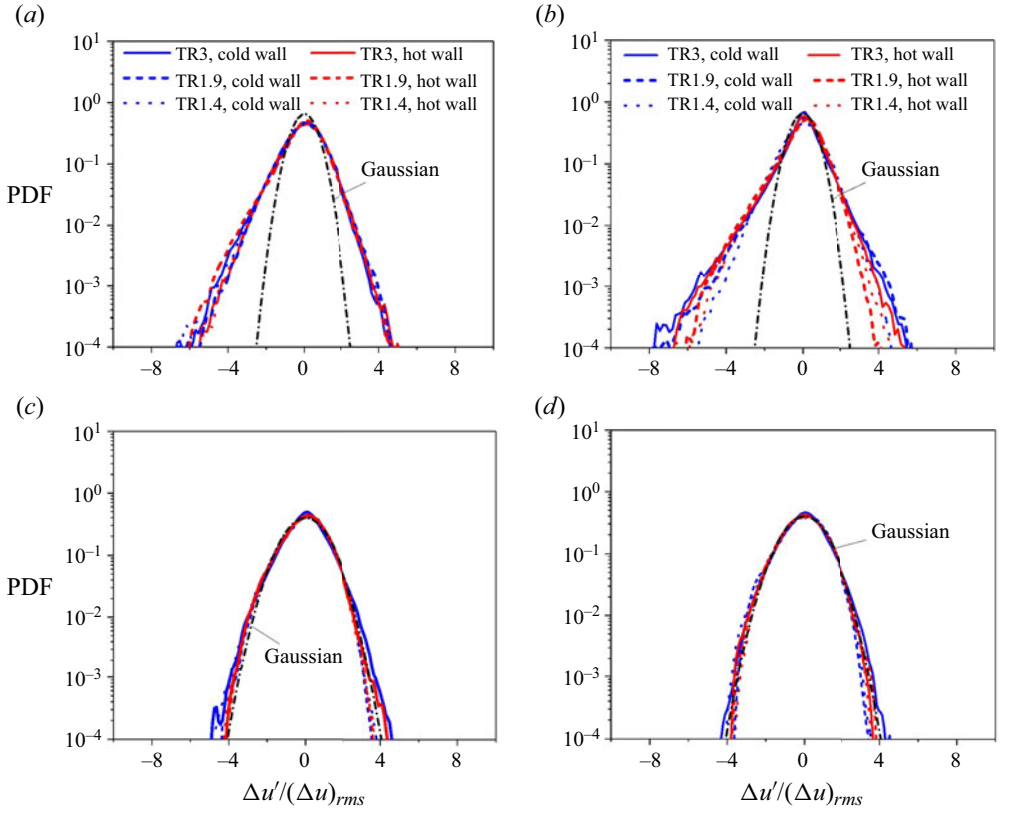

Figure 3. Profiles for PDFs of longitudinal velocity increments $\Delta u' = u'(x + r, y, z) - u'(x, y, z)$ near both walls for different cases: (*a*) $r = \Delta x$ at $\zeta^* = 300$ in the LIR, where Δx is the streamwise grid spacing; (*b*) $r = \Delta x$ at $\zeta^* = 10$; (*c*) $r = 20\Delta x$ at $\zeta^* = 300$; (*d*) $r = 100\Delta x$ at $\zeta^* = 300$. The x-axis is rescaled by the r.m.s. of velocity increments. The blue curves indicate cold wall profiles, the red curves correspond to hot wall profiles and black dashed lines denote the Gaussian distribution.

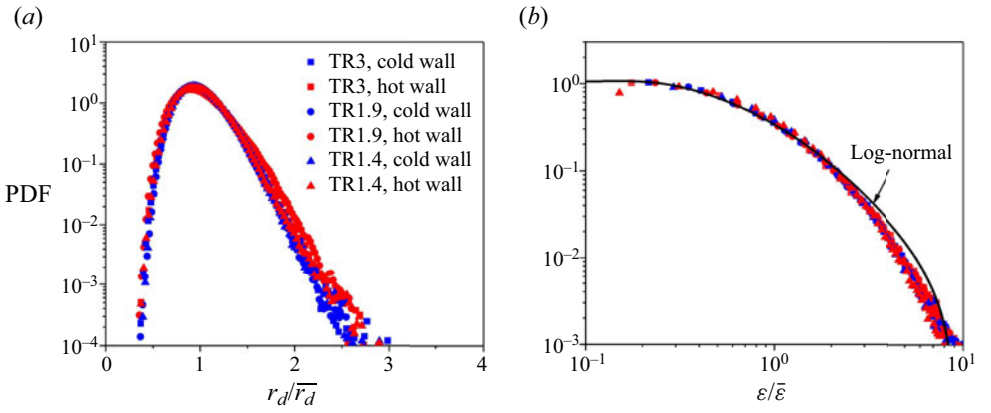

Figure 4. The PDFs of (*a*) local dissipation scales and (*b*) dissipation rate in the LIR (at $\zeta^* = 300$) of the channel for different cases: blue lines, cold wall profiles; red lines, hot wall profiles; black line, the log-normal fitting $\mathrm{PDF}_{\varepsilon/\bar{\varepsilon}} = y_0 + (A/(\sqrt{2\pi}(\varepsilon/\bar{\varepsilon})\sigma))\exp[-(\ln((\varepsilon/\bar{\varepsilon})/x_c))^2/2\sigma^2]$ with $y_0 = -0.00436$, $x_c = 0.682$, $\sigma = 1.232$, $A = 1.102$.

We display the PDFs of local dissipation scale r_d and local dissipation rate $\varepsilon/\bar{\varepsilon}$ near the cold wall and the hot wall in figure 4. The local dissipation scale, r_d, is determined such that $\bar{\rho}(\Delta u')_{r_d} r_d/\bar{\mu} = 1$ (Schumacher 2007; Hamlington *et al.* 2012), with $(\Delta u')_{r_d}$ the streamwise velocity-fluctuation increments over the streamwise distance r_d. Thus, the PDFs of local dissipation scale can formally be written as $P[r_d|0.9 \leq \bar{\rho}(\Delta u')_{r_d} r/\bar{\mu} \leq 1.1]$ (Hamlington *et al.* 2012). It should be noted that the Kolmogorov scale, $\bar{\eta} = [(\bar{\mu}/\bar{\rho})^3 \bar{\rho}/\bar{\varepsilon}]^{1/4}$, only results from the dimensional analysis and may contain the length scales at the dissipative range and the inertial range. According to Hamlington *et al.* (2012), including only values of r_d in the above definition of local dissipation scale can ensure the isolation of the flow structures occurring at the cutoff of dissipative range and inertial range. Knowledge of the PDFs of the local dissipation scales, given in figure 4, provides evidence of the similarity of the characteristic length scale at the dissipative range for transcritical flows. Figure 4(*a*) shows $\mathrm{PDF}(r_d)$ at $\zeta^* = 300$ for all cases. It can be seen that there are only small differences in $\mathrm{PDF}(r_d/\overline{r_d})$ among cases, suggesting that $\mathrm{PDF}(r_d/\overline{r_d})$ in the LIR of the channel is insensitive to the real-fluid variable-property effects. Similar observations can be made from figure 4(*b*), showing that the PDFs of dissipation rate, $\mathrm{PDF}(\varepsilon/\bar{\varepsilon})$ approximately follows the log-normal distribution for $0.1 < \varepsilon/\bar{\varepsilon} < 2$, but deviates from the log-normal distribution for the extreme events at the tail. In the locally isotropic region, despite the different levels of density and viscosity fluctuations in the flows, the PDFs of the dissipation rate have similar profiles; our observations support the consistency of the local dissipation scale for transcritical cases.

Results of the second-order structure function (S_2) of u' for the LIR of the channel give similar insights into the small-scale flow structures. Figure 5 presents the longitudinal structure functions of fluctuating streamwise velocity $S_2 = \overline{[u'(x+r, y, z) - u'(x, y, z)]^2}$ as a function of the streamwise spatial increment in the LIR of the channel for TR3. There is reasonable collapse of the distributions in the dissipative range with $r < 20\bar{\eta}$. In the LIR of the channel, the inertial region of S_2 normalized by the mean dissipation rate (see figure 5*a*) and that normalized by the local dissipation rate (considering intermittency, see figure 5*b*) have not yet been observed in either case due to the Reynolds number not being sufficiently large. In the dissipative range, according to Kolmogorov's first similarity

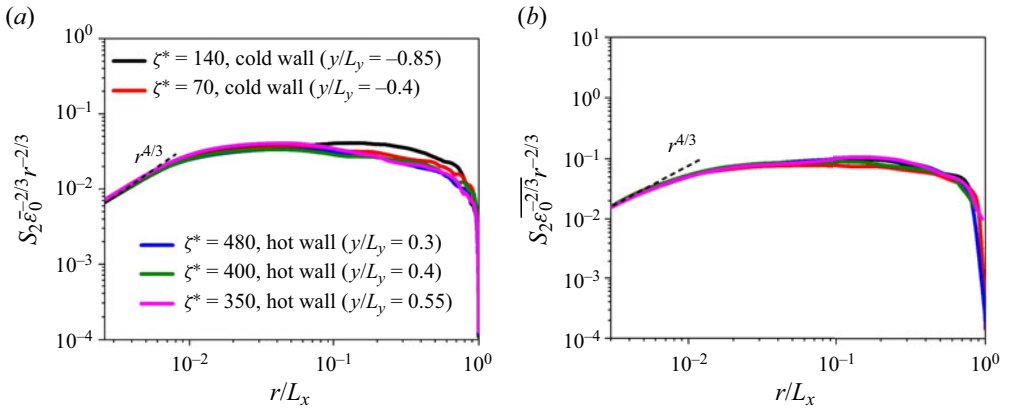

Figure 5. Second-order structure functions of u' ($S_2 = \overline{[u'(x+r,y,z) - u'(x,y,z)]^2}$) as a function of streamwise spatial increment in the LIR of the channel for TR3: (*a*) S_2 rescaled by the mean dissipation rate $\bar{\varepsilon}_0$; (*b*) S_2 rescaled by local dissipation rate (ε_0 averaged over the streamwise two-point distance).

hypothesis, the viscosity and dissipation rate dominate the structure function. A simple dimensional analysis yields the expression of the second-order structure function

$$S_2 = C_2 \left(\frac{\bar{\rho}\bar{\varepsilon}_0}{\bar{\mu}} \right) r^2, \tag{3.5}$$

with C_2 the second-order structure function coefficient, and $\varepsilon_0 = \varepsilon/\rho$. Equation (3.5) indicates that the second-order structure function for transcritical flows is consistent with that of the incompressible flows given in Pope (2000). In summary, despite the small discrepancies at the tail of the $\partial u'/\partial x$-PDF profiles, the low-order structure functions of u' for all cases have the same scaling in the dissipative range.

3.3. *Real-fluid effects on moments of small-scale statistics*

The moments of the velocity gradients and dissipation rate play an important role for characterizing the small-scale dynamics. The *n*th-order moments of turbulent statistics can be written as

$$M_n(Z) = \frac{\overline{Z^n}}{(\overline{Z^2})^{n/2}}, \tag{3.6}$$

with Z denoting any flow quantity. Figure 6(*a*,*b*) shows the variations of the skewness of the velocity gradient ($Z = \partial u'/\partial x$, $n = 3$ in (3.6)) and the flatness of the velocity gradient ($Z = \partial u'/\partial x$, $n = 4$ in (3.6)) as a function of ζ^* for all cases. It can be seen that $M_3(\partial u'/\partial x)$ (i.e. $S_{\partial u'/\partial x}$) and $M_4(\partial u'/\partial x)$ (i.e. $F_{\partial u'/\partial x}$) away from the wall are nearly constant. Distributions of $S_{\partial u'/\partial x}$ or $F_{\partial u'/\partial x}$ are qualitatively similar for all the wall flows, with minor quantitative variations. As the distance to the wall increases, $S_{\partial u'/\partial x}$ decreases, reaches a minimum, increases and finally forms a plateau in the outer region of the flow. This behaviour is also consistent with that of incompressible flows with moderate and high Re_τ reported in Djenidi *et al.* (2017). We can also observe the characteristic behaviour of $F_{\partial u'/\partial x}$ for all transcritical cases, it is found that $F_{\partial u'/\partial x}$ approaches a constant, which is independent of the thermal property changes. In Appendix C, we examine the results based on density-weighted velocity fluctuations, and confirm that the results of density-weighted velocity-fluctuation derivatives are consistent with the Reynolds-averaged results.

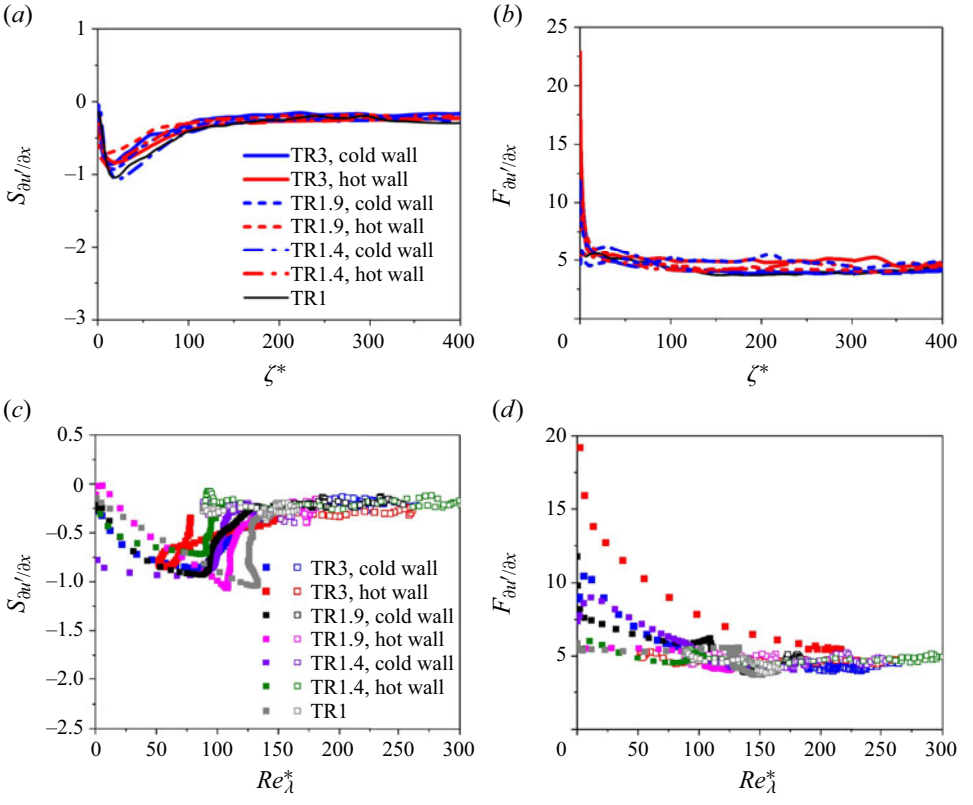

Figure 6. Moments of fluctuating streamwise velocity gradients (see (3.6)) in different cases: (*a*) $Z = \partial u'/\partial x$, $n = 3$ (skewness) as a function of ζ^*; (*b*) $Z = \partial u'/\partial x$, $n = 4$ (flatness) as a function of ζ^*; (*c*) $Z = \partial u'/\partial x$, $n = 3$ (skewness) as a function of semilocal Taylor Reynolds number Re^*_λ; (*d*) $Z = \partial u'/\partial x$, $n = 4$ (flatness) as a function of Re^*_λ. In (*c*) and (*d*), open symbols represent the results in the LIR of the channel whereas solid symbols indicate the near-wall layers; blue, near the cold wall for TR3; red, near the hot wall for TR3; black, near the cold wall for TR1.9; pink, near the hot wall for TR1.9; purple, near the cold wall for TR1.4; green, near the hot wall for TR1.4; grey, TR1.

We make two additional remarks here. First, the data from Abe, Antonia & Kawamura (2009) showed that the plateau of the velocity gradient skewness did not occur for $Re_\tau = 180$, while this plateau can be clearly observed in the LIR of the channel when Re_τ reaches 590 for incompressible flows (Vreman & Kuerten, 2014). Our results also indicate that at transcritical conditions, the plateau where $S_{\partial u'/\partial x}$ and $F_{\partial u'/\partial x}$ remain constant definitely exists when Re_τ exceeds 300 (i.e. the lowest Re_τ in the present study); this supports that $S_{\partial u'/\partial x}$ and $F_{\partial u'/\partial x}$ in the LIR of the channel are independent of ζ^* when Re_τ exceeds 300, which is approximately consistent with the Re_τ threshold for $S_{\partial u'/\partial x} = \text{const.}$ and $F_{\partial u'/\partial x} = \text{const.}$ for incompressible turbulence. Second, in the LIR of the channel, the level of agreement of $S_{\partial u'/\partial x}$ and $F_{\partial u'/\partial x}$ between the present study and the previous studies on incompressible channel flows (Abe *et al.* 2009; Vreman & Kuerten 2014; Tang *et al.* 2015; Antonia *et al.* 2017; Tang *et al.* 2019) is relatively poor. Abe *et al.* (2009) reported that $S_{\partial u'/\partial x} = -0.6$ in the outer layer for $Re_\tau = 395$ and 640 (comparable magnitude with the present study) while $S_{\partial u'/\partial x}$ remains less than -0.5 according to Vreman & Kuerten (2014). Xu, Antonia & Rajagopalan (2001) found that $S_{\partial u'/\partial x}$ and $F_{\partial u'/\partial x}$ remain -0.53 and 10 at $Re_\lambda > 200$–300 in the outer layer of incompressible

plane jet and circular jet. The current transcritical cases suggest that $S_{\partial u'/\partial x}$ and $F_{\partial u'/\partial x}$ converge at similar Re_τ and Re_λ compared with incompressible flows (i.e. $Re_\tau = 300$–600 or $Re_\lambda = 200$–300). However, the corresponding values of the $S_{\partial u'/\partial x}$ and $F_{\partial u'/\partial x}$ plateau ($S_{\partial u'/\partial x} = -0.25$ and $F_{\partial u'/\partial x} = 4$) are different from those of incompressible flows, which means that the discrepancies between transcritical flows and incompressible flows are mainly associated with the effects of real-fluid property variations, while the Reynolds number effect contributes only minimally. Note that even for TR1 for which the two walls have the same temperature and heat, transfer is weak, although the boundary condition is similar to that of incompressible flows, the small-scale statistics still differ from the incompressible flows. The small pressure fluctuations in the flow also lead to large thermal property changes, leading to Re^*_λ varying from 700 at the wall to 1000 at the centreline and thus turbulence dynamics depart significantly from incompressible flows. This may explain the differences of the $S_{\partial u'/\partial x}$ and $F_{\partial u'/\partial x}$ profiles between TR1 and incompressible flows studied in the prior studies (Abe *et al.* 2009; Vreman & Kuerten 2014; Tang *et al.* 2015; Antonia *et al.* 2017; Tang *et al.* 2019).

Next we assess the behaviour of $S_{\partial u'/\partial x}$ and $F_{\partial u'/\partial x}$ in terms of Taylor Reynolds number (see figure 6*c*,*d*; $Re^*_\lambda = \bar{\rho} u' \lambda / \bar{\mu}$ is semilocal Taylor Reynolds number defined based on the local density and viscosity along the wall-normal direction). In the context of K41 (Kolmogorov 1941), both S and F in incompressible flows are approximately independent of Re_λ; whereas in K62 (Kolmogorov 1962; Obukhov 1962), S and F are expected to increase with increasing Re_λ. To clearly distinguish the profiles in the LIR of the channel, we use different symbols to identify different wall-normal positions in the channels. Figure 6(*c*,*d*) shows that the universality of skewness and flatness of fluctuating streamwise velocity gradients with Re^*_λ in the locally isotropic region (see the open symbols) manifests primarily. Moreover, in all cases, $S_{\partial u'/\partial x}$ in the LIR is nearly independent of Re^*_λ, providing support for K41 at transcritical conditions; $S_{\partial u'/\partial x}$ becomes constant when $Re^*_\lambda > 150$ (as shown in figure 6*c*). These conclusions bear analogies with those for incompressible flows in which $S_{\partial u'/\partial x}$ becomes independent of Re_λ when $Re_\lambda > 100$ for jet flows (Tang *et al.* 2019) and when $Re_\lambda > 150$ for wall-bounded flows (Djenidi *et al.* 2017) (note that $Re_\lambda \equiv Re^*_\lambda$ for incompressible flows). With regard to $F_{\partial u'/\partial x}$, we find that in the LIR of the channel for transcritical flows, $F_{\partial u'/\partial x}$ remains approximately constant for $100 < Re^*_\lambda < 300$ (see the open symbols in figure 6*d*). For incompressible flows, results of isotropic flows and jet flows (van Atta & Antonia 1980; Kerr 1985; Sreenivasan & Antonia 1997) show that $F_{\partial u'/\partial x}$ varies slightly with Re_λ when $Re_\lambda < 100$, and then increases monotonically with Re_λ for $Re_\lambda \in (10^2, 10^3)$. However, Djenidi *et al.* (2017) pointed out that the plateau of F occurs when Re_λ reaches 100–500 in wall-bounded flows. According to the above discussions, $F_{\partial u'/\partial x}$ for transcritical wall-bounded flows also exhibits consistency with the incompressible wall flows.

According to K41 and K62, the consistency of the small-scale statistics for incompressible cases is only valid for sufficiently large Reynolds numbers. From the results of figures 3–6, we conclude that the moments of the velocity gradients with order $n \leq 4$ follow the universal behaviours (thought to exist only at very high Reynolds numbers) in the presence of real-fluid thermodynamic property variations even at relatively moderate Reynolds numbers.

In figure 7, we show the moments of the local dissipation rate $\overline{\varepsilon^n}/\bar{\varepsilon}^n$ as a function of $\zeta*$ in the LIR for transcritical channel flows. The dissipation moments $\overline{\varepsilon^n}/\bar{\varepsilon}^n$ reflect the variations in the smallest dissipative scale, particularly for high n (Hamlington *et al.* 2012). Similar to the results for incompressible channel flows (Hamlington *et al.* 2012), the low-order moments of ε remain constant in the locally isotropic region (see figure 7*a*).

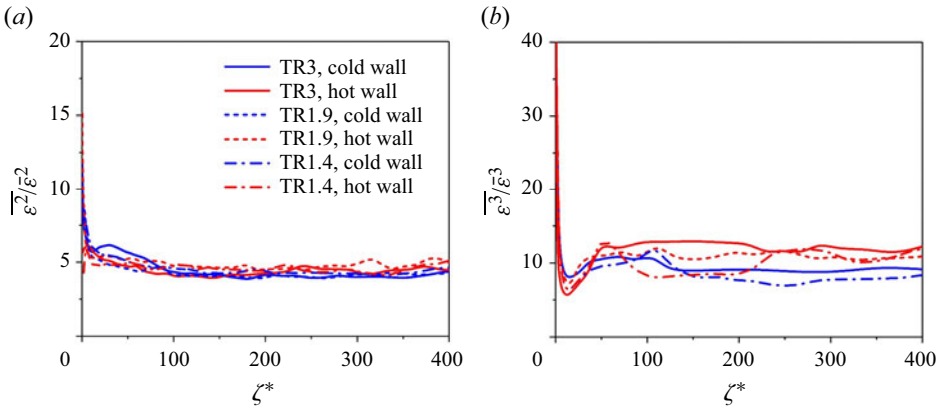

Figure 7. Variations of local dissipation rate moments $\overline{\varepsilon^n}/\bar{\varepsilon}^n$ as functions of $\zeta*$ for different cases: (*a*) $n=2$; (*b*) $n=3$.

In contrast, the high-order dissipation rate moments ($n=3$) obey different behaviours (see figure 7*b*); the interesting point is that the high-order dissipation rate moments do not collapse in the LIR of the channel. The variable-property effects on high-order small-scale statistical moments will be elaborated on in the following section.

3.4. *Real-fluid effects on small-scale high-order statistical moments*

Our analysis shows that low-order moments of small-scale statistics such as dissipative length scale, dissipation rate and the velocity gradient have universal behaviours at transcritical conditions. However, the high-order moments of small-scale statistics in transcritical flows are sensitive to real-fluid property variations. To clarify the modulations of these effects on the moments of velocity gradients and dissipation rate, we consider the following budget equation for local dissipation rate at transcritical conditions (Li *et al.* 2023):

$$\varepsilon = \underbrace{\bar{\mu}\frac{\partial u_i'}{\partial x_j}\left(\frac{\partial u_i'}{\partial x_j}+\frac{\partial u_j'}{\partial x_i}\right)}_{\varepsilon_I} \underbrace{-\frac{2}{3}\bar{\mu}(\boldsymbol{\nabla}\cdot\boldsymbol{u'})^2}_{\varepsilon_{II}} + \underbrace{\mu'\frac{\partial u_i'}{\partial x_j}\left(\frac{\partial \bar{u}_i}{\partial x_j}+\frac{\partial \bar{u}_j}{\partial x_i}-\frac{2}{3}\frac{\partial \bar{u}_k}{\partial x_k}\delta_{ij}\right)}_{\varepsilon_{III}} + \underbrace{\frac{\partial u_i'}{\partial x_j}\left[\mu'\left(\frac{\partial u_i'}{\partial x_j}+\frac{\partial u_j'}{\partial x_i}-\frac{2}{3}\frac{\partial u_k'}{\partial x_k}\delta_{ij}\right)\right]}_{\varepsilon_{IV}}, \tag{3.7}$$

where ε_I is the solenoidal term composed of the mean viscosity and the enstrophy, ε_{II} denotes the dilatational term related to the fluctuating velocity divergence, ε_{III} and ε_{IV} are budgets related to the fluctuations of viscosity. In our previous study (Li *et al.* 2023), we found that turbulent dissipation is dominated by the solenoidal term, which means that the dissipation rate is primarily generated by vorticity and the contributions from thermal property fluctuations are negligible. For incompressible flows, we can expect $\varepsilon_{II}=\varepsilon_{III}=\varepsilon_{IV}=0$ and thus $\varepsilon=\varepsilon_I$. In the LIR of the channel, (3.1) is valid so that

$$\bar{\varepsilon} = 15\bar{\mu}\overline{\left(\frac{\partial u'}{\partial x}\right)^2}. \tag{3.8}$$

According to (3.8), we can establish the relation between the dissipation rate moments and velocity gradient moments,

$$\frac{\overline{\varepsilon^n}}{\bar{\varepsilon}^n} = \frac{\overline{15^n \bar{\mu}^n \left(\frac{\partial u'}{\partial x}\right)^{2n}}}{\overline{15^n \bar{\mu} \left(\frac{\partial u'}{\partial x}\right)^{2}}^n} = \frac{\overline{\left(\frac{\partial u'}{\partial x}\right)^{2n}}}{\overline{\left(\frac{\partial u'}{\partial x}\right)^{2}}^n} = M_{2n}\left(\frac{\partial u'}{\partial x}\right). \tag{3.9}$$

Equations (3.9) shows that the skewness and flatness of velocity gradients are associated with the local dissipation rate moments in the LIR for channel flows. As discussed above, the PDFs of the longitudinal velocity gradient distribute similarly in the locally isotropic region of the channel, leading to the universal profiles of low-order dissipation rate moments, as shown in figure 7(*a*). However, as in Belin, Maurer & Willaime (1997), the discrepancy at the exponential-decaying low-probability tails can contribute significantly to high-order moments, resulting in the substantial discrepancies of high-order moments for different conditions. Figure 8 further shows the high-order structure functions. In figure 8(*a*), we first examine the profiles of the rescaled longitudinal structure function of the streamwise velocity $S_{2n}(r)/r^{2n}$ ($n \leq 4$). The plateau of $S_{2n}(r)/r^{2n}$ at small-scale is visible, thus it follows $S_{2n}(r) \sim r^{2n}$ in the dissipative range. In light of the definition of $S_{2n}(r)$, we have the following relation in the dissipative range:

$$\frac{S_2}{r^2} = \overline{\left(\frac{\partial u'}{\partial x}\right)^2}, \quad \frac{S_{2n}}{r^{2n}} = \overline{\left(\frac{\partial u'}{\partial x}\right)^{2n}}, \tag{3.10a,b}$$

and thus,

$$M_{2n}\left(\frac{\partial u'}{\partial x}\right) = \frac{\overline{\left(\frac{\partial u'}{\partial x}\right)^{2n}}}{\overline{\left(\frac{\partial u'}{\partial x}\right)^{2}}^n} = \frac{S_{2n}}{S_2^n} = \frac{C_{2n}\left(\frac{\bar{\rho}\bar{\varepsilon_0}}{\bar{\mu}}\right)^n r^{2n}}{C_2^n \left(\frac{\bar{\rho}\bar{\varepsilon_0}}{\bar{\mu}}\right)^n r^{2n}}. \tag{3.11}$$

Equation (3.11) yields

$$M_{2n}\left(\frac{\partial u'}{\partial x}\right) = \frac{S_{2n}}{S_2^n} = \frac{C_{2n}}{C_2^n}. \tag{3.12}$$

Equation (3.11) indicates that the moments of the velocity gradient are determined by the structure functions in the dissipative range. Figure 8(*b*) gives the rescaled longitudinal structure function of the streamwise velocity $S_{2n}(r)/(u_\tau^*)^{2n}$ at the channel centreline for TR1 and TR3. It is evident that as the order of the structure function (n) increases, the structure functions with the same order for different cases cannot collapse in the dissipative range, even though they still have the same scaling exponent with r. According to (3.12), the inconsistency of S_{2n}/S_2^n between TR3 and TR1 indicates that the high-order structure function coefficient C_{2n} varies due to the variable-property effects in the channels (it is worth noting that in the context of incompressible turbulence, the structure function coefficient for a certain order is a constant), which essentially leads to the discrepancy of high-order moments of velocity gradient and dissipation rate in the LIR at transcritical conditions. Figure 8(*c*) shows PDFs of moments of local dissipation rate at $\zeta^* = 300$ near the hot wall for different cases. The PDFs of high-order dissipation rate for all cases cannot collapse, suggesting that the high-order moments of small-scale quantities are strongly

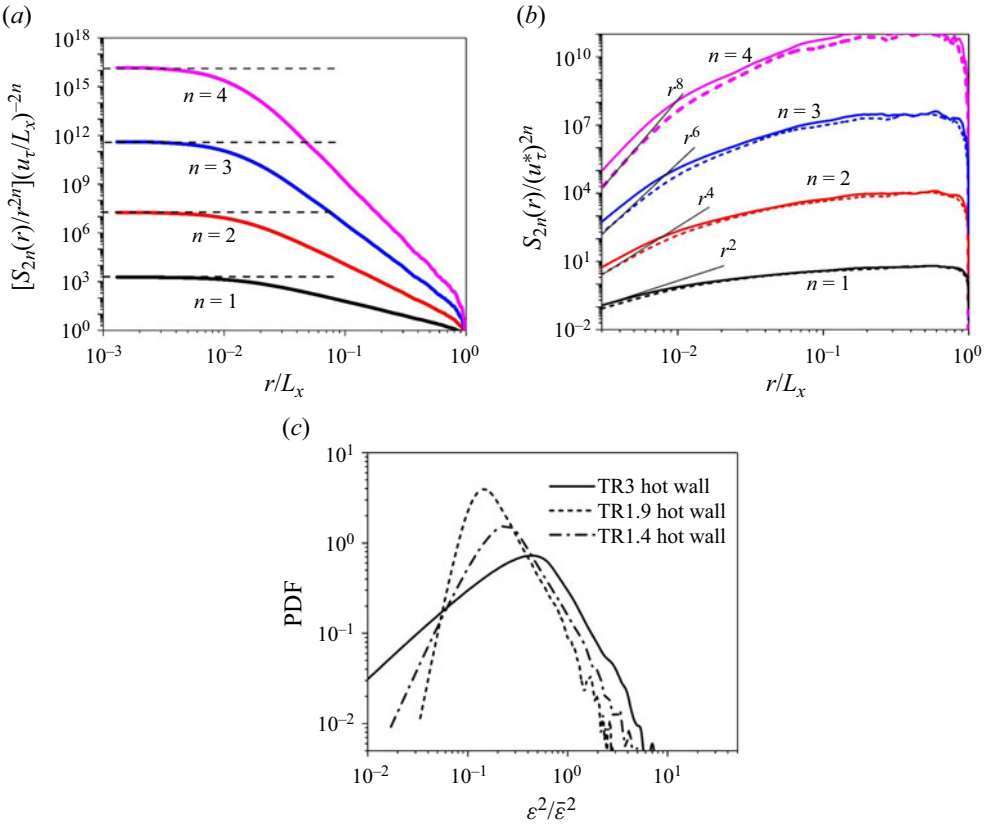

Figure 8. Variable-property effects on small-scale high-order statistics: (*a*) the longitudinal structure functions of the streamwise velocity $S_{2n}(r)/r^{2n} = \overline{(\Delta u')^{2n}}/r^{2n}$ $(n \leq 4)$ rescaled by $(u_{\tau,cold}/L_x)^{-2n}$ at the channel centreline of TR3. The horizontal lines are defined by the converged value of the corresponding curves; (*b*) rescaled longitudinal structure function of the streamwise velocity $S_{2n}(r)/(u_\tau^*)^{2n}$ at the channel centreline in TR1 (solid lines) and TR3 (dashed lines), with S_{2n} rescaled by u_τ^* at the centreline of TR3; (*c*) PDFs of local dissipation rate moment $\varepsilon^2/\bar{\varepsilon}^2$ at $\zeta^* = 300$ near the hot wall for all cases.

sensitive to changes in thermal properties. Recalling that the PDF profiles of $\partial u'/\partial x$ do not collapse at the tail, we expect that the rare events with high velocity gradients and turbulent dissipation contribute significantly to the discrepancies of high-order moments of dissipation rate between different cases.

3.5. *Real-fluid effects on the scalings for small-scale statistics*

This section examines the real-fluid effects on the scalings for small-scale statistics, including the structure function and dissipation rate moments. According to Kolmogorov's second hypothesis, S_n is independent of the viscosity in the inertial range (Kolmogorov 1941; Pope 2000), and hence dimensional analysis yields

$$S_n \sim r^{\zeta_n}. \tag{3.13}$$

Several models have been proposed for the intermittency factor ζ_n for locally isotropic flows at incompressible conditions, such as the refined similarity hypothesis (K62)

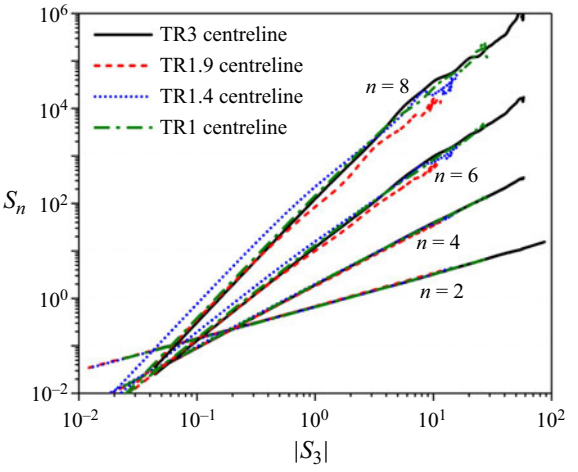

Figure 9. Plots of longitudinal structure functions of streamwise velocity (S_2, S_4, S_6 and S_8) as a function of $|S_3|$ at the centreline of the channel for all cases.

(Kolmogorov 1962; Obukhov 1962),

$$\zeta_n = \frac{1}{3}n\left[1 - \frac{1}{6}\mu(n-3)\right], \quad \mu = 0.25, \tag{3.14}$$

and the universal scaling law (SL94) (She & Leveque 1994)

$$\zeta_n = \frac{n}{9} + 2\left[1 - \left(\frac{2}{3}\right)^{n/3}\right]. \tag{3.15}$$

Equations (3.14) and (3.15) were developed by considering the intermittency of the dissipation rate at high Reynolds number. Benzi *et al.* (1993) reported on the existence of an extended self-similarity (ESS) that holds for high and low Reynolds numbers, which is characterized by the universal scaling exponents of the structure functions with the independence of the Reynolds number. The ESS reads (Benzi *et al.* 1993)

$$\overline{|u'(x+r,y,z) - u'(x,y,z)|^n} \propto (|S_3|)^{\zeta_n}. \tag{3.16}$$

Obviously $\overline{|u'(x+r,y,z) - u'(x,y,z)|^n} = S_n$ when n is even. Since the Re_τ and Re_λ considered in our study are relatively moderate, we use the ESS hypothesis to study the scaling for intermittency. Figure 9 shows plots of S_2, S_4, S_6 and S_8 as a function of the third-order structure function at the centreline for all conditions. For $n = 2$ and 4 (figure 9*a*,*b*), the results of all cases collapse onto a single profile which exhibits reasonably good agreement with the power law, even if no inertial range is established. Furthermore, self-similarity extends far beyond the inertial range deep into the dissipation range. We note that ζ_n in the LIR of the channel is insensitive to the wall-normal location (not shown here for brevity). These results show that the ESS exists at transcritical conditions for low-order structure functions. As n increases (see $n = 6$ and $n = 8$ shown in figure 9*c*,*d*), the profiles for S_n cannot collapse, suggesting that the ESS can hardly be applied for high-order structure functions and ζ_n becomes dependent on the real-fluid variable-property effects.

In table 3, we show the fitted value of ζ_n for $n = 2$–8 at transcritical conditions based on ESS, along with the coefficients of determination. The values of ζ_n are determined by

	ζ_n			
N	TR3	TR1.9	TR1.4	TR1
2	0.685	0.687	0.683	0.688
4	1.296	1.295	1.295	1.292
5	1.574	1.575	1.566	1.567
6	1.836	1.842	1.813	1.827
7	2.084	2.097	2.042	2.077
8	2.323	2.345	2.261	2.32

Table 3. The fitted ζ_n based on ESS for $n = 2$–8 in all transcritical flows.

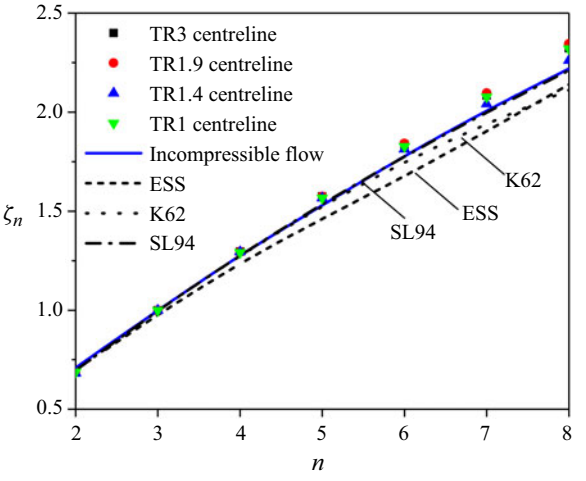

Figure 10. Scaling exponents ζ_n based on ESS computed for $n = 2$–8 at transcritical conditions for different cases. For comparison, the predictions of ζ_n by K62 (Kolmogorov 1962), SL94 (She & Leveque 1994), incompressible ESS (Benzi *et al.* 1993) and the experimental results of ζ_n in the locally isotropic flow for incompressible condition (the blue line, She & Leveque 1994) are also demonstrated.

fitting the data in the region of $|S_3| < 20$, in which the structure functions closely follow the exponential law. The coefficients of determination (R^2) are higher than 0.99, implying the accuracy of the fitted results. To gain more insights into the real-fluid variable-property effects on the intermittency, we present ζ_n based on ESS computed for $n = 2$–8 at transcritical conditions in figure 10, with the predictions of ζ_n by K62 (Kolmogorov 1962), SL94 (She & Leveque 1994) and incompressible ESS model (Benzi *et al.* 1993) included. It is shown that ζ_n in the locally isotropic region of transcritical flows is higher than that of incompressible flows. Moreover, the noticeable difference is observed between ζ_n at transcritical conditions and that obtained by ESS for incompressible flow, implying again that the turbulent intermittency is largely affected by the real-fluid variable-property effects at transcritical conditions. Evidently, the modulations on intermittency are more significant for the higher-order structure functions.

The underlying mechanisms for intermittent behaviour are substantiated by means of visualizing the structures related to the rare events. Instantaneous isosurfaces of wall-normal velocity fluctuations as well as corresponding flooded contours of density in the locally isotropic region near the cold wall for TR1.9 and TR1.4 are shown in figure 11. The isosurfaces of wall-normal velocity fluctuations with $v'' = 2.5$ m s^{-1} and $v'' = 1.2$ m

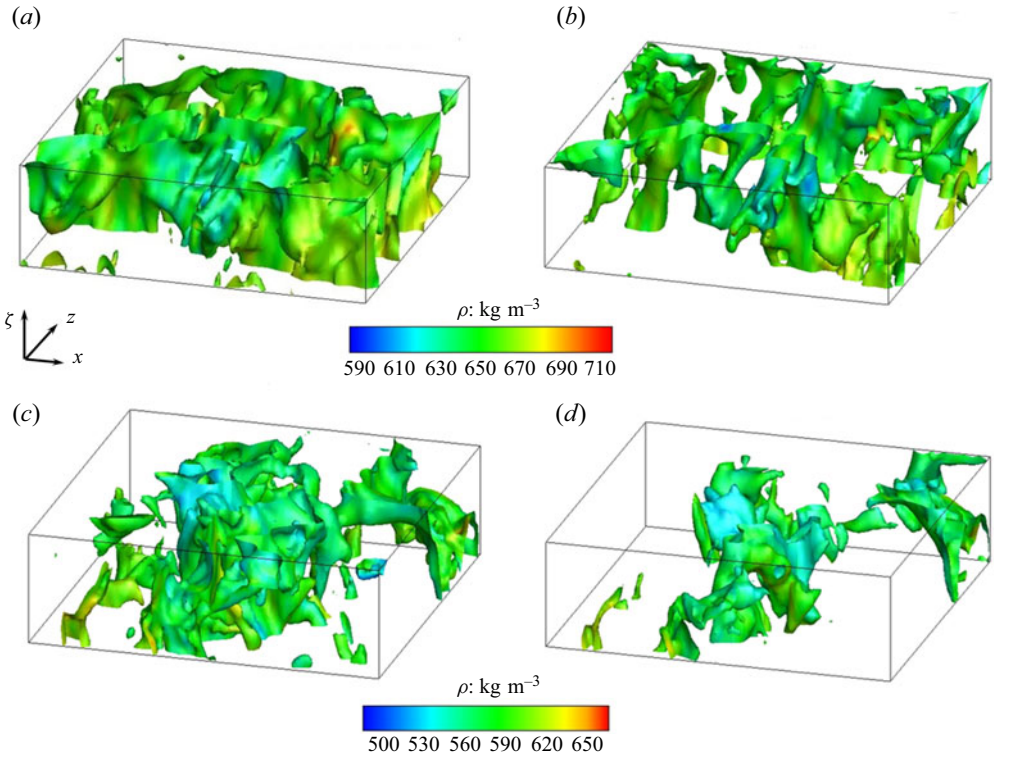

Figure 11. Isosurfaces of wall-normal velocity fluctuation coloured by the instantaneous density in the locally isotropic region near the cold wall, with $v'' = 1.2$ m s^{-1} in (*a*,*c*) and $v'' = 2.5$ m s^{-1} in (*b*,*d*); here (*a*,*b*) TR1.9 and (*c*,*d*) TR1.4.

s^{-1} are associated with the rare structures with $\rho > 680$ kg m^{-3} for TR1.9, corresponding to the mean density value in the buffer layer. This implies clear ejection events from the near-wall layers as the near-wall turbulence lifts up the dense fluid in the buffer layer into the locally isotropic region with lower density. However, for TR1.4 with lower density ratio, such high-density rare structures from the near-wall layer are not obvious. This implies attenuated ejection motion of the rare structures with decreasing real-fluid thermodynamic effects in the channel. Evidently, these wall-normal coherent motions lead to significant mixing in the channel, resulting in effective momentum and energy transport between the near-wall layer and locally isotropic region. The comparison between the flow structures of TR1.9 and TR1.4 leads us to conclude that the ejection motions and turbulent mixing in the channel are enhanced as the increasing real-fluid effects. Since the ejected fluids from the near-wall layer have much lower density and tend to have higher velocity, their mixing with the core results in significant velocity increments in the locally isotropic layer and creates extreme events for high velocity gradients. This is a unique characteristic of transcritical wall-bounded flows which explains the extreme, rare events for high velocity gradients displayed in figure 3. Thus, the real-fluid variable-property effects play a first-order role in modulating the PDFs of higher-order structure functions and dissipation rate by introducing extreme, rare events for high velocity gradients; consequently, the higher-order structure function and its intermittency behave differently from those for incompressible flows.

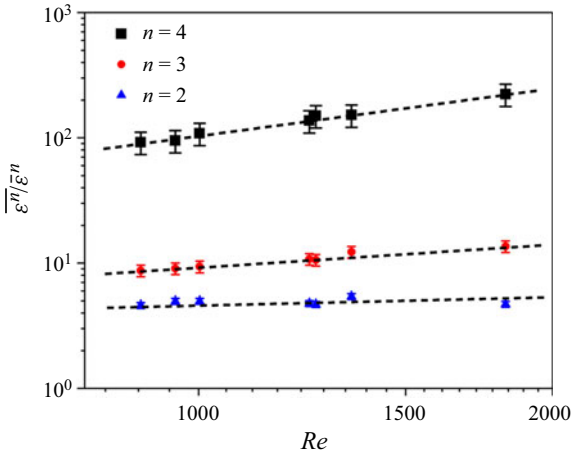

Figure 12. Scaling of dissipation rate moments against global Re for $n = 2$–4 in all cases (i.e. TR3 hot wall, TR3 cold wall, TR1.9 hot wall, TR1.9 cold wall, TR1.4 hot wall, TR1.4 cold wall and TR1). Here, $Re = \rho_w U' L_y/\mu_w$ with U' the r.m.s. of fluctuation velocity, $U' = \overline{(u'^2 + v'^2 + w'^2)}^{1/2}$ and L_y the half-height of the channel. The results of dissipation rate moments and Re are obtained by averaging the data within the whole LIR in the channel. Each symbol represents a separate flow case.

To provide more quantitative insights into the high-order moments of small-scale quantities, we compare the global Re dependence of local dissipation rate moments for different flows in figure 12. The global Re is defined as $Re = \rho_w U' L_y/\mu_w$ with U' the r.m.s. of fluctuation velocity, $U' = \overline{(u'^2 + v'^2 + w'^2)}^{1/2}$ and L_y the half-height of the channel (Hamlington *et al.* 2012; Schumacher *et al.* 2014). Note that here the dissipation rate moments and Re are obtained by averaging the data over the whole LIR in the channel (Hamlington *et al.* 2012; Schumacher *et al.* 2014). The scaling relation for the moments of the energy dissipation rate was derived from a theory for incompressible homogeneous and isotropic turbulence (Yakhot & Sreenivasan 2005; Yakhot 2006). It is given by

$$\overline{\varepsilon^n} \propto Re^{d_n}, \quad d_n = n + \frac{\theta_{4n}}{\theta_{4n} - \theta_{4n+1} - 1}. \tag{3.17}$$

Here, θ_n is the inertial-range scaling exponent of the nth-order moment of the velocity increment $\Delta u'$. The error bar of 90 % confidence limits is also estimated and shown in figure 12 following a moving-block bootstrap method (Garcia, Jackson & Garcia 2005; Hamlington *et al.* 2012). The normalized dissipation moments are calculated in each snapshot over x–z planes, and the block sizes used to estimate the error bar are equal to one flow-through time, which is defined as $L_x/\overline{u_b}$ with $\overline{u_b}$ being the bulk velocity. The interesting point is that despite the different levels of density and viscosity fluctuations in the flows, the nth-order dissipation rate moments for all cases follow the same scaling law ($\overline{\varepsilon^n}/\bar{\varepsilon}^n \sim Re^{d_n}$), strongly suggesting that the high-order energy dissipation statistics vary universally with Re at transcritical conditions. By fitting the scaling laws for each n (see dashed lines in figure 12), we find that the scaling exponents for the dissipation rate moments are $d_2 = 0.104$, $d_3 = 0.622$ and $d_4 = 1.237$. Calculations of these exponents for incompressible homogeneously isotropic turbulence were shown to give $d_2 = 0.152$, $d_3 = 0.476$ and $d_4 = 0.978$ (Yakhot 2006; Schumacher 2007); Hamlington *et al.* (2012) reported that the local dissipation rate for incompressible channel flows follows the same scaling as that for isotropic flows. Our results show that although the dissipation rate

moments at transcritical conditions collapse to the same scaling, the scaling exponents are different from those for incompressible channel flows and isotropic flows. For lower values of n (such as $n = 2$), the small-scale moments remain nearly constants in the LIR of the channel, thus the scaling exponents of dissipation rate moments for transcritical flows are lower than those predicted by the incompressible isotropic turbulence theory (Yakhot 2006; Schumacher 2007); as n increases (e.g. $n = 3$ and 4), the variable-property effects start to influence the dissipation rate moments and thus d_n exceeds those for incompressible flows.

4. Conclusions

According to incompressible turbulence theory, small-scale quantities such as dissipation rate, local dissipation scale and velocity gradients should have universal behaviours. In this work, we study effects of real-fluid property variations on small-scale characteristics of transcritical wall-bounded turbulence to investigate if the universality of the small-scale dynamics in incompressible turbulence can be extended to transcritical flow regimes. Our main conclusions are summarized as follows.

In the LIR of the channel, the longitudinal velocity gradient and dissipation rate have universal PDF distributions at moderate Reynolds number. There are only small differences at the tail of PDFs of local dissipation length scale and dissipation rate for different cases. These results strongly suggest that the universal behaviour for low-order statistics of small-scale quantities also extends to transcritical flows. This universality persists for all transcritical cases considered in the present study and only vanishes in the near-wall region with strong anisotropy. In addition, we can also observe the characteristic behaviours of skewness and flatness of velocity gradient in all transcritical cases. It is found that in the LIR of the channel, $S_{\partial u'/\partial x}$ and $F_{\partial u'/\partial x}$ in all cases approach the constant value of -0.25 and 4, respectively. With regard to the $S_{\partial u'/\partial x}$-$Re^*_\lambda$ and $F_{\partial u'/\partial x}$-$Re^*_\lambda$ relations, we find that $S_{\partial u'/\partial x}$ and $F_{\partial u'/\partial x}$ profiles behave universally in the locally isotropic region for all transcritical cases; $S_{\partial u'/\partial x}$ and $F_{\partial u'/\partial x}$ in the LIR are independent of Re^*_λ, providing support for K41 at transcritical conditions and exhibiting consistency with incompressible wall-bounded flows.

In contrast, the high-order moments of dissipation rate and velocity gradients in the LIR for all channel flow cases do not collapse. This inconsistency of high-order statistics among transcritical cases originates from intermittent, rare events indicated by the scattered tail of the velocity-derivative PDF profiles and the varying higher-order structure function coefficient. The traditional models of intermittency, such as K62 and SL94, are invalid at transcritical conditions. The intermittency factor for lower-order structure functions at transcritical conditions follows the ESS, while the higher-order structure functions and their intermittency behave differently from those for incompressible flows. The real-fluid thermodynamic properties enhance the momentum and energy transport induced by the ejection motion from the buffer layer, modulating the PDFs of higher-order structure functions and dissipation rate by introducing the extreme, rare events for high velocity gradients. The dissipation rate moments in all transcritical flows follow a universal scaling with Re, but the scaling exponents are different from those in incompressible flows, as demonstrated in the present study by the Re-scaling of the moments of local dissipation rate.

Results of the present work are helpful for establishing further evidence for the universality of small-scale turbulent statistics in the presence of strongly varying thermodynamic conditions. Since we have shown the consistency of small-scale quantities between the transcritical flows and incompressible flows, there is also considerable merit

in developing universal scaling laws and parameterizations of small-scale quantities for transcritical flows in the context of incompressible, low-Reynolds-number turbulence.

Acknowledgements. We thank Dr S. Tang from Shenzhen Graduate School, Harbin Institute of Technology and Dr J. Guo from Lawrence Livermore National Laboratory for their helpful recommendations.

Funding. F.L. is funded by China Postdoctoral Science Foundation, grant no. 2023M742845 and National Funded Postdoctoral Research Project, grant no. GZB20230978. W.Z. is funded by National Natural Science Foundation of China, grant no. 92152301. M.I. is funded by the US Department of Energy Office of Science with Award DE-SC0022222.

Declaration of interests. The authors report no conflict of interest.

Author ORCIDs.
Fangbo Li https://orcid.org/0000-0003-0982-3823;
Weiwei Zhang https://orcid.org/0000-0001-7799-833X;
Matthias Ihme https://orcid.org/0000-0002-4158-7050.

Appendix A. Governing equations and equation of state for DNS

The DNS database used in this study consists of the channel flow with two isothermal walls which have been conducted in our prior studies (Ma *et al.* 2018; Guo *et al.* 2022; Li *et al.* 2023). The governing equations of mass, momentum and total energy for a fully compressible flow are solved in conservative form,

$$\frac{\partial \rho}{\partial t} + \frac{\partial (\rho u_i)}{\partial x_i} = 0, \tag{A1}$$

$$\frac{\partial (\rho u_i)}{\partial t} + \frac{\partial (\rho u_i u_j)}{\partial x_j} = -\frac{\partial p}{\partial x_i} + \frac{\partial \tau_{ij}}{\partial x_j} + f_i, \tag{A2}$$

$$\frac{\partial (\rho E)}{\partial t} + \frac{\partial}{\partial x_j}[u_j(\rho E + p)] = \frac{\partial}{\partial x_j}(u_i \tau_{ij} - q_j) + u_i f_i, \tag{A3}$$

where $u_i = (u,\ v,\ w)$ denotes the streamwise, wall-normal and spanwise components of the velocity, t is the time, p is the pressure, E is the total energy per unit mass, f_i is the ith component of the body force vector which acts as a streamwise-homogeneous pressure gradient to impose a prescribed bulk streamwise momentum. Following Huang *et al.* (1995) which focused on the compressible, isothermal channel flows, f_i is given as

$$f_i = -\frac{\sum \tau_w}{2L_y}\frac{\bar{\rho}}{\rho_0}\delta_{1i}, \tag{A4}$$

where ρ_0 is the volume-averaged density and δ_{ij} is the Kronecker delta operator. The viscous stress tensor τ_{ij} and heat flux vector q_i are given as

$$\tau_{ij} = \mu\left(\frac{\partial u_i}{\partial x_j} + \frac{\partial u_j}{\partial x_i}\right) - \frac{2}{3}\mu\frac{\partial u_k}{\partial x_k}\delta_{ij}, \tag{A5}$$

$$q_i = -\lambda\frac{\partial T}{\partial x_i}, \tag{A6}$$

with λ is the thermal conductivity. According to Miller *et al.* (2001), Ma *et al.* (2018), Kim *et al.* (2019) and Guo *et al.* (2022), the PR equation (Peng & Robinson 1976) can be employed as the EoS to calculate the physical properties of N_2 at high-pressure

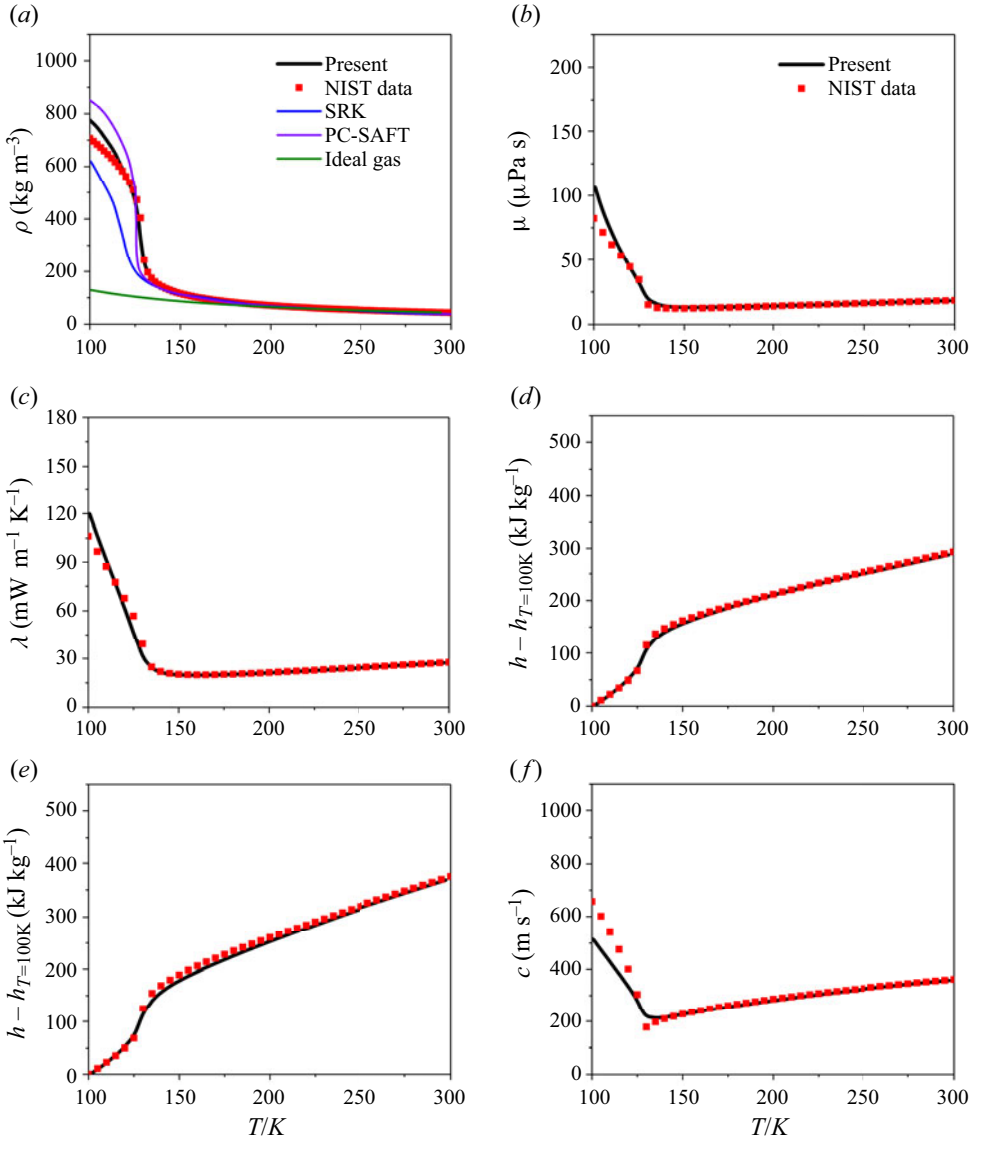

Figure 13. The thermodynamic and transport properties as a function of temperature obtained in the present DNS, with the comparisons with NIST data ($p_r = 1.14$ for N_2) included: (*a*) density ρ, computed profiles are provided for various commonly-used equations of state, including PR model (used in present work), ideal gas model, Soave–Redlich–Kwong (SRK) model and the perturbed chain statistical associating fluid theory (PC-SAFT); (*b*) dynamic viscosity μ; (*c*) thermal conductivity λ; (*d*) enthalpy difference $h - h_{T=100\mathrm{K}}$, with $h_{T=100\mathrm{K}}$ the enthalpy at $T = 100$ K; (*e*) internal energy difference $h - h_{T=100\mathrm{K}}$, with $h_{T=100\mathrm{K}}$ the internal energy at $T = 100$ K; (*f*) speed of sound c.

transcritical conditions because of its high accuracy in predicting thermodynamic variables in the vicinity of the critical point. The PR EoS reads

$$p = \frac{\rho RT}{1 - b\rho} - \frac{\rho^2 a}{1 + 2b\rho - b^2\rho^2}, \tag{A7}$$

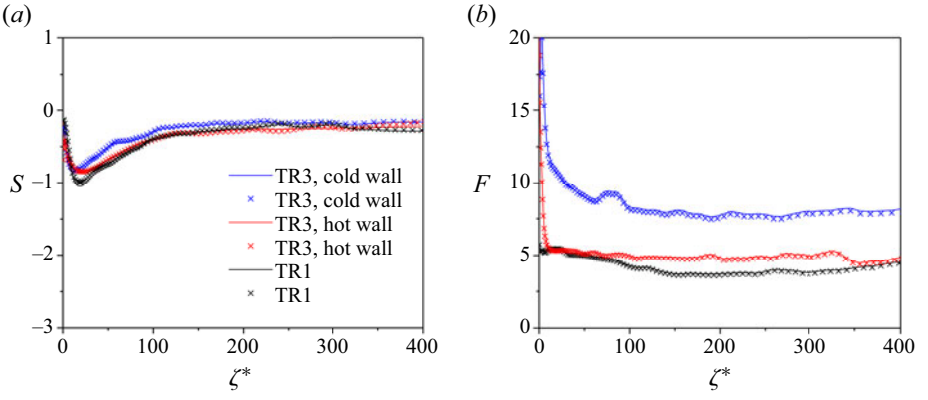

Figure 14. Plots of (*a*) $S_{\partial u'/\partial x}$ and (*b*) $F_{\partial u'/\partial x}$ of grid refinement results for TR3 and TR1. For clarity, the results near the TR3 cold wall in (*b*) are multiplied by 2. Lines, the current grid $N_x \times N_y \times N_z = 384 \times 256 \times 384$; symbols, the fine grid $N_x \times N_y \times N_z = 543 \times 356 \times 543$.

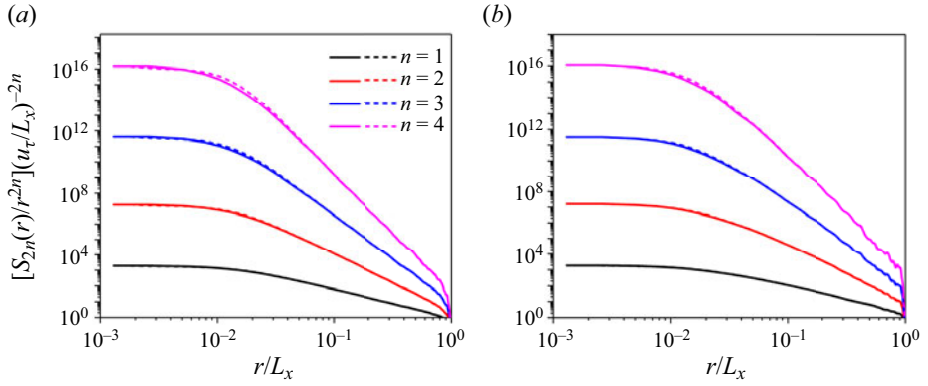

Figure 15. The structure functions of the streamwise velocity fluctuations rescaled by $u_{\tau,cold}/L_x$ at the channel centreline for (*a*) TR3 and (*b*) TR1. Solid lines, the current grid $N_x \times N_y \times N_z = 384 \times 256 \times 384$; dashed lines, the fine grid $N_x \times N_y \times N_z = 543 \times 356 \times 543$.

$$a = 0.457236\frac{R^2T_c^2}{p_c}\left[1 + c\left(1 - \sqrt{\frac{T}{T_c}}\right)\right]^2, \tag{A8}$$

$$b = 0.077796\frac{RT_c}{p_c}, \tag{A9}$$

with

$$c = 0.37464 + 1.54226\omega - 0.26992\omega^2, \tag{A10}$$

and with $\omega = 0.0372$ being the acentric factor. For N_2, $b = 8.58 \times 10^{-4}$ and $c = 0.432$. The internal energy E and enthalpy h are expressed as

$$E = E_0(T) + \int_0^\rho \left[\frac{p}{\rho^2} - \frac{T}{\rho^2}\left(\frac{\partial p}{\partial T}\right)_\rho\right] \mathrm{d}\rho, \tag{A11}$$

$$h = E + \frac{p}{\rho}, \tag{A12}$$

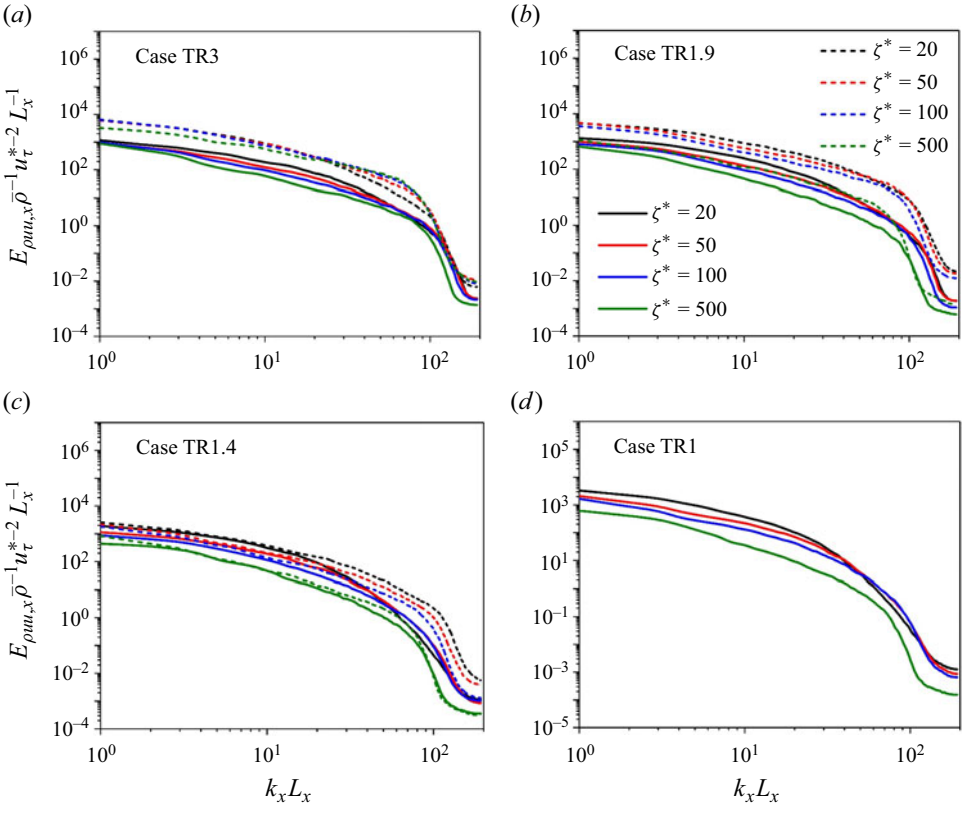

Figure 16. Streamwise energy spectra $E_{\rho uu,x}$ versus streamwise wavenumber k_x. Here, $E_{\rho uu,x}$ has been normalized by the mean density $\bar{\rho}$ and the semilocal friction velocity u_τ^*. Solid lines indicate the cold wall profiles while dashed lines indicate the hot wall profiles.

where $E_0(T)$ is the reference internal energy for ideal gas. Many studies have verified the accuracy of the PR EoS at high-pressure transcritical conditions (Miller *et al.* 2001; Hickey *et al.* 2013; Sengupta *et al.* 2017; Kim *et al.* 2019). The transport properties (viscosity μ and thermal conductivity λ) are evaluated by Chung's model for high-pressure fluids (Chung *et al.* 1988; Congiunti, Bruno & Giacomazzi 2003; Hickey *et al.* 2013). The accuracy of these models for predicting transport properties of transcritical fluids in DNS studies has been examined in the literature (Congiunti *et al.* 2003; Hickey *et al.* 2013; Ma *et al.* 2018; Kim *et al.* 2019; Toki *et al.* 2020; Guo *et al.* 2022; Li *et al.* 2023). The dynamic viscosity μ (in units of P) is computed as (Chung *et al.* 1988; Poling, Prausnitz & O'Connell 2001; Kim *et al.* 2019)

$$\mu = \mu_k + \mu_p, \tag{A13}$$

$$\mu_k = \mu_0\left(\frac{1}{G_2} + A_6 Y\right), \tag{A14}$$

$$\mu_p = \left[36.344 \times 10^{-6}\frac{(M_w T_c)^{1/2}}{V_c^{2/3}}\right] A_7 Y^2 G_2 \exp\left(A_8 + \frac{A_9}{T^*} + \frac{A_{10}}{T^{*2}}\right), \tag{A15}$$

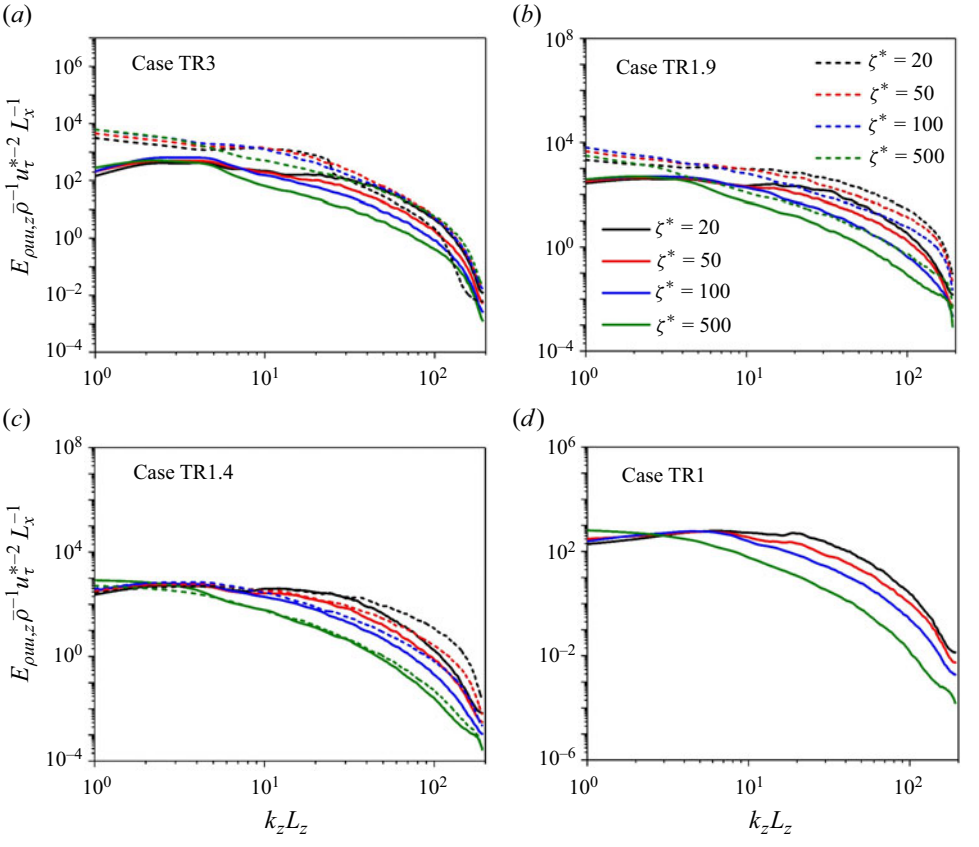

Figure 17. Spanwise energy spectra $E_{\rho uu,z}$ versus spanwise wavenumber k_z. Here $E_{\rho uu,z}$ has been normalized by the mean density $\bar{\rho}$ and the semilocal friction velocity u_τ^*. Lines as in figure 16.

$$\mu_0 = (4.0785 \times 10^{-5})\frac{(M_wT)^{1/2}}{V_c^{2/3}\Omega^*}F_c, \tag{A16}$$

$$F_c = 1 - 0.2756\omega + 0.059035\mu_r^4 + \kappa, \tag{A17}$$

$$\Omega^* = \frac{A}{T^{*B}} + \frac{C}{\exp(DT^*)} + \frac{E}{\exp(FT^*)} + GT^{*B}\sin(ST^{*W} - H), \tag{A18}$$

$$T^* = 1.2593T/T_c, \tag{A19}$$

$$G_2 = \frac{A_1[1 - \exp(-A_4Y)]/Y + A_2G_1\exp(A_5Y) + A_3G_1}{A_1A_4 + A_2 + A_3}, \tag{A20}$$

$$G_1 = \frac{1 - 0.5Y}{(1 - Y)^3}, \tag{A21}$$

$$Y = \frac{1}{6}\rho V_c, \tag{A22}$$

$$A_i = a_{0,i} + a_{1,i}\omega + a_{2,i}\mu_r^4 + a_{3,i}\kappa, \tag{A23}$$

$$\mu_r = 131.3\frac{\chi}{(V_cT_c)^{1/2}}, \tag{A24}$$

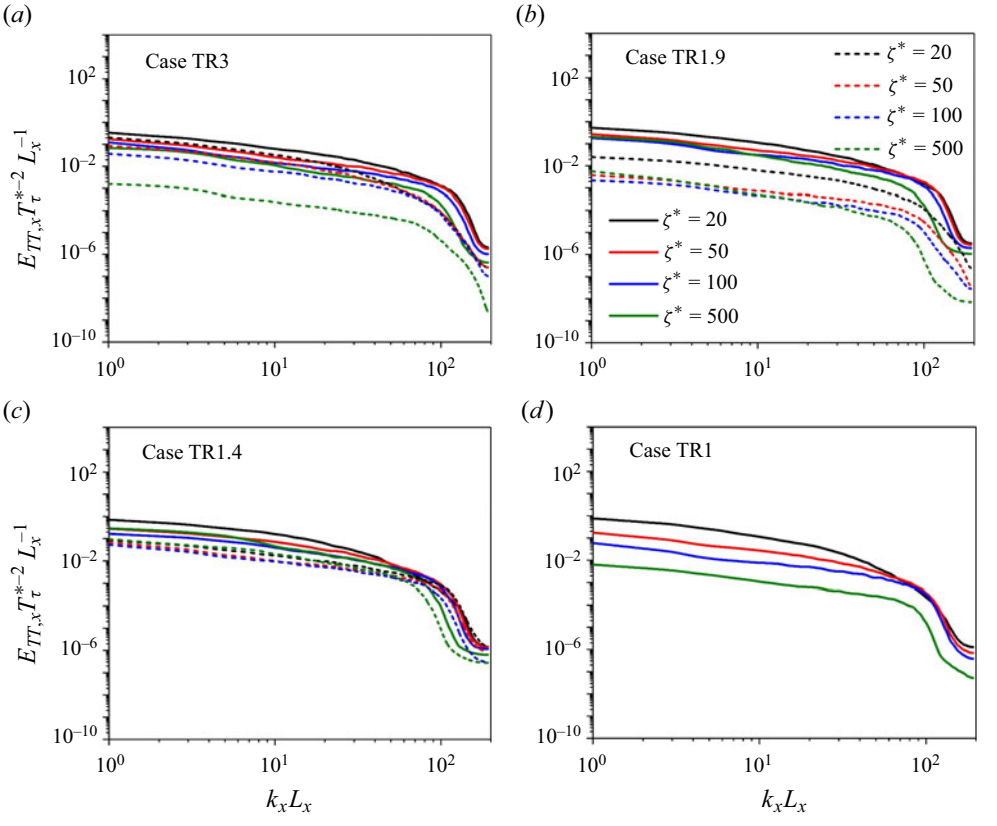

Figure 18. Streamwise temperature spectra $E_{TT,x}$ versus streamwise wavenumber k_x. Here, $E_{TT,x}$ is normalized by the mean density $\bar{\rho}$ and the semilocal friction temperature T_τ^*. Lines as in figure 16.

where M_w is the molecular weight in g mol^{-1}, T is the temperature in K, V_c is the critical volume in cm^3 mol^{-1}, μ_0 is the low-pressure gas viscosity in P, Ω^* is the reduced collision integral which depends on the intermolecular potential, F_c is a factor to account for molecular structure and polar effects, χ is a dimensionless dipole moment of molecules, ω is the acentric factor and κ is a correction factor for hydrogen-bonding effect of associating substances such as alcohols, acids and water. For non-polar gases such as N_2, only the two first terms in (A18) are used since the other two terms become zero. The thermal conductivity (in W m^{-1} K^{-1}) is developed by the following approach (Chung *et al.* 1988; Poling *et al.* 2001; Kim *et al.* 2019):

$$\lambda = \lambda_k + \lambda_p, \tag{A25}$$

$$\lambda_k = \lambda_0 \left(\frac{1}{H_2} + B_6 Y \right), \tag{A26}$$

$$\lambda_0 = 31.2 \frac{\mu_0}{M_w'} \psi, \tag{A27}$$

$$\lambda_p = \left[3.586 \times 10^{-3} \frac{(T_c/M_w')^{1/2}}{V_c^{2/3}} \right] B_7 Y^2 T_r^{1/2} H_2, \tag{A28}$$

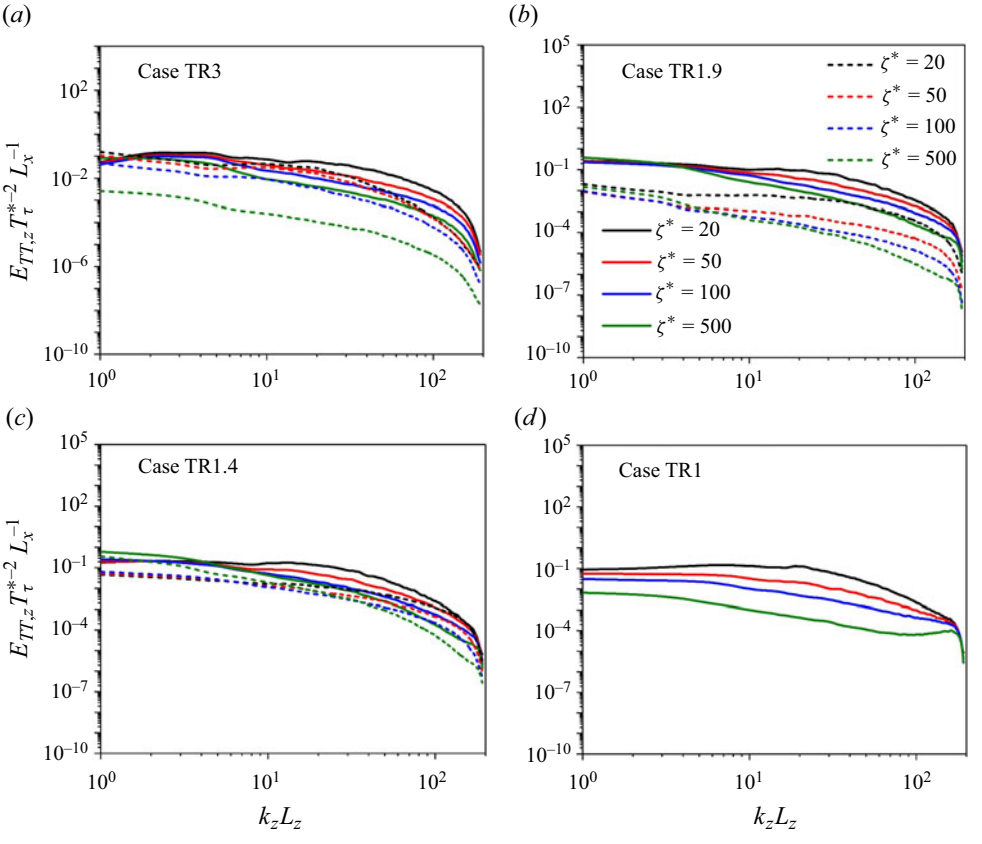

Figure 19. Spanwise temperature spectra $E_{TT,z}$ versus spanwise wavenumber k_z. Here $E_{TT,z}$ is normalized by the mean density $\bar{\rho}$ and the semilocal friction temperature T_τ^*. Lines as in figure 16.

$$\psi = 1 + \alpha \frac{0.215 + 0.28288\alpha - 1.061\beta + 0.26665Z}{0.6366 + \beta Z + 1.061\alpha\beta}, \tag{A29}$$

$$H_2 = \frac{B_1[1 - \exp(-B_4 Y)]/Y + B_2 G_1 \exp(B_5 Y) + B_3 G_1}{B_1 B_4 + B_2 + B_3}, \tag{A30}$$

$$B_i = b_{0,i} + b_{1,i}\omega + b_{2,i}\mu_r^4 + b_{3,i}\kappa, \tag{A31}$$

$$\alpha = \frac{C_v}{R} - \frac{3}{2}, \tag{A32}$$

$$\beta = 0.7862 - 0.7109\omega + 1.3168\omega^2, \tag{A33}$$

$$Z = 2 + 10.5T_r^2, \tag{A34}$$

where M_w' is the molecular weight in kg mol^{-1}, $M_w' = M_w/10^3$, T is the temperature in K, V_c is the critical volume in cm^3 mol^{-1}, μ_0 is the low-pressure gas viscosity shown in (A16) while here its unit is Pa s. The values of the coefficients in (A13)–(A34) can be found in Poling *et al*. (2001).

Figure 13 shows the thermodynamic and transport properties as a function of temperature obtained in the present DNS. As seen, the PR EoS performs well in capturing the near-Widom-line gradient in ρ as well as in capturing the quantitative density values for

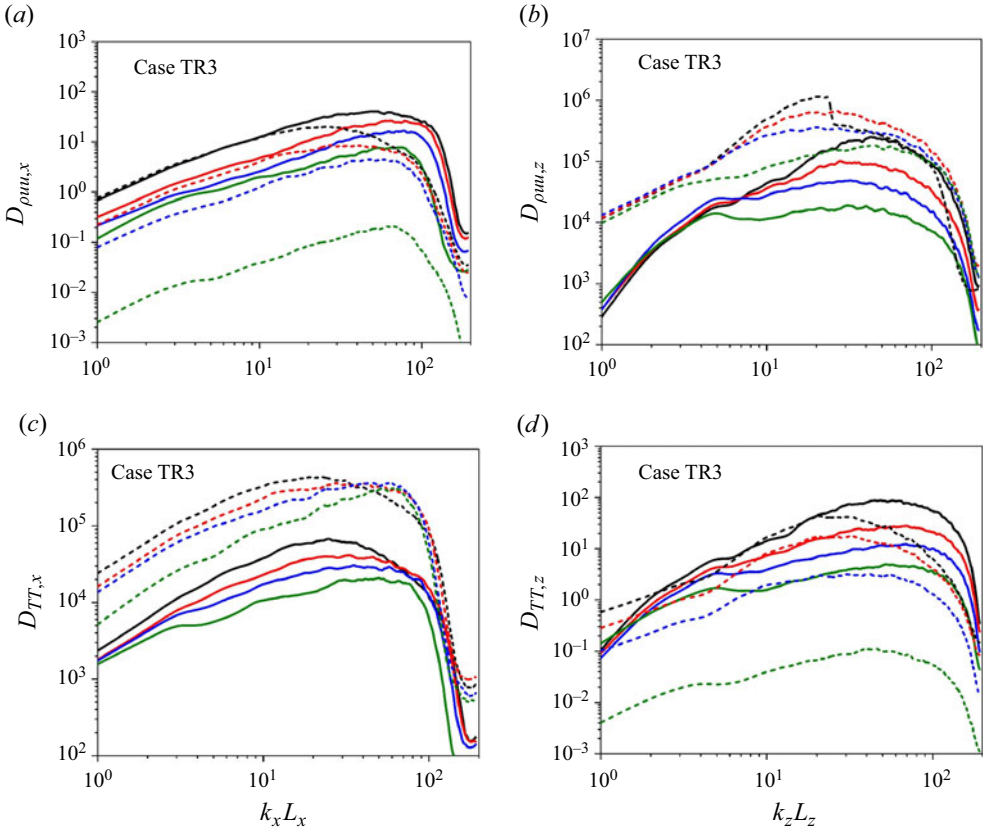

Figure 20. Plots of dissipation spectra for streamwise momentum and temperature fluctuations versus wavenumber for TR3. Lines as in figure 16.

the present thermodynamic conditions ($p_r = 1.14$, $T \in [100\ \text{K}, 300\ \text{K}]$). The comparisons with NIST data show that the mean relative error of PR EoS and Chung's model are within 1 % for $p_r = 1.14$, $T \in [100\ \text{K}, 300\ \text{K}]$. Furthermore, Peng & Robinson (1976) reported the r.m.s. error less than 1.25 % in predicting enthalpy at transcritical conditions that are comparable to those used in our investigation; the errors of similar level were also reported by Congiunti *et al.* (2003) and Hickey *et al.* (2013) for predicting ρ of high-pressure transcritical fluids. For transport properties, the agreement between Chung's model and experimental values is quite good and the mean relative errors are usually below 5 % for $p_r < 2$ (Poling *et al.* 2001); and the accuracy of Chung's model for predicting λ and μ of transcritical fluids has also been verified in Congiunti *et al.* (2003). Particularly, the possibility of calculating thermal properties with a single method with several common expressions makes the method by Chung's model the most effective in terms of computational times and accuracy for computational fluid dynamics (Congiunti *et al.* 2003). However, we note that the present models exhibit deviations of the order of 5 %–10 % from the NIST data for ρ, μ and λ at 100–110 K. In summary, our validations and past studies generally confirm the accuracy of the models of thermal properties employed in the present study.

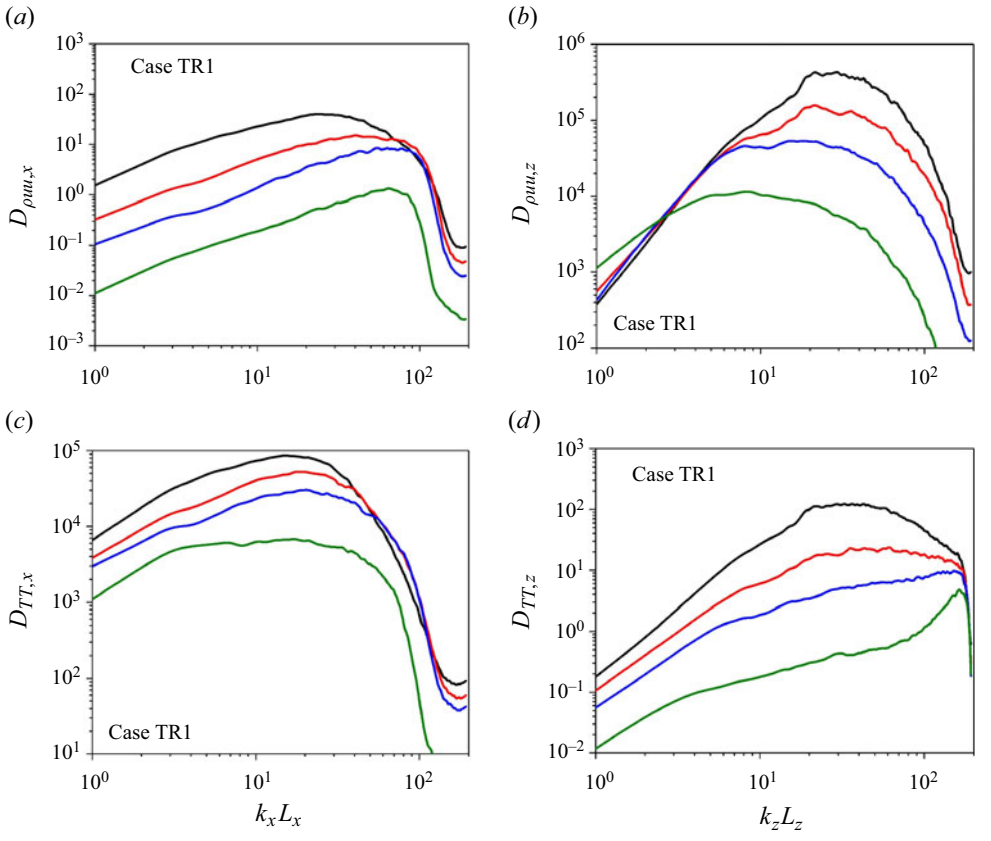

Figure 21. Plots of dissipation spectra for streamwise momentum and temperature fluctuations versus wavenumber for TR1. Lines as in figure 16.

Appendix B. The grid resolutions

As part of the set-up of the channel DNS used in the current investigation, Ma *et al*. (2018) performed a grid convergence study for case TR3 and evaluated the results. In Appendix B we show additional grid resolution studies for skewness, kurtosis and higher-order moments of velocity gradient. Two grid resolutions for TR3 and TR1 are used in this grid convergence study: a 'regular grid' that is the same as used in the current study with $N_x \times N_y \times N_z = 384 \times 256 \times 384$ for a total of 37.7×10^6 control volumes and a 'fine grid', with $N_x \times N_y \times N_z = 543 \times 356 \times 543$ for a total of 105×10^6 control volumes. Plots of $S_{\partial u'/\partial x}$, $F_{\partial u'/\partial x}$ and higher-order structure functions of grid refinement results for TR3 and TR1 are given in figures 14 and 15 to demonstrate the grid resolutions. The results of skewness and kurtosis of velocity gradient are consistent between different grids to within 3 %. For the results of higher-order structure functions at the channel centreline shown here, no significant difference is seen among the different grids, thus confirming adequate grid convergence. From the totality of these findings presented for grid convergence, we conclude that the computational grid used for the current simulations satisfies the requirements to be of DNS resolution for small-scale velocity statistics with the order lower than 8.

As presented in figures 16–19, to ensure that the relevant small scales are sufficiently resolved, we show the streamwise and spanwise energy spectra for momentum ($E_{\rho uu}$) and

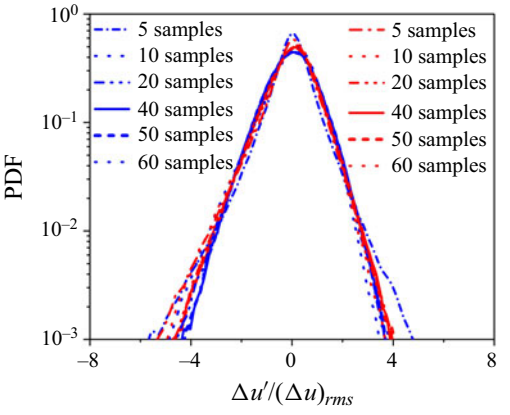

Figure 22. Sensitivity of PDFs of streamwise velocity gradient on the number of statistical samples. Blue lines, $\zeta^* = 100$ near the cold wall for TR3; red lines, $\zeta^* = 100$ near the hot wall for TR3.

temperature (E_{TT}) as a function of streamwise wavenumber k_x and spanwise k_z using the mesh with $N_x \times N_y \times N_z = 384 \times 256 \times 384$. If the small-scales are under-resolved, the energy spectra will usually increase towards the grid cutoff (Ma *et al.* 2018; Kim *et al.* 2019; Guo *et al.* 2022). All profiles roll off rapidly, with no build-up of spectra occurring at high wavenumbers, providing evidence of the adequacy of the resolution of the small scale for both the hydrodynamic and thermodynamic quantities. Furthermore, figures 20 and 21 show the one-dimensional dissipation spectra of momentum fluctuations and temperature fluctuations,

$$D_{\rho uu}(k) = 2\frac{\bar{\mu}}{\bar{\rho}}k^2 E_{\rho uu}\bar{\rho}^{-1}u_\tau^{*-2}L_x^{-1}, \tag{B1}$$

$$D_{TT}(k) = 2\frac{\bar{\mu}}{\bar{\rho}}k^2 E_{TT}T_\tau^{*-2}L_x^{-1}, \tag{B2}$$

here the plots for TR3 and TR1 are shown to assess the resolution of the small-scales for the largest and smallest density changes across all cases. For both momentum and enthalpy, at least three decades of dissipation spectra can be resolved. The peak of dissipation spectra (and the premultiplied spectra) is visible at all wall-normal locations. At the dissipative scale of dissipation spectra in figures 20 and 21, the build-up of the curves appears quite minimal, which is consistent with the energy spectra observed in Kim *et al.* (2019). These results support the well-resolvedness of the dissipative scale required for calculating the results of small-scale moments in this study.

Here we address the sensitivity of small-scale statistics on the number of statistical samples. As presented in § 2.2, we average over homogeneous directions and time using data in 20 flow-through times to obtain the statistics, with one flow-through time being $L_x/\overline{u_b}$. That corresponds to ∼50 time slices for calculating the statistics. To examine the effects of samples number on small-scale statistics, we show the sensitivity of PDFs of velocity gradient on the number of samples for TR3 in figure 22. Converged results for PDFs of velocity gradient can be obtained when averaging over 50 time slices, implying the small-scale results are not affected by the samples number and the statistical noises.

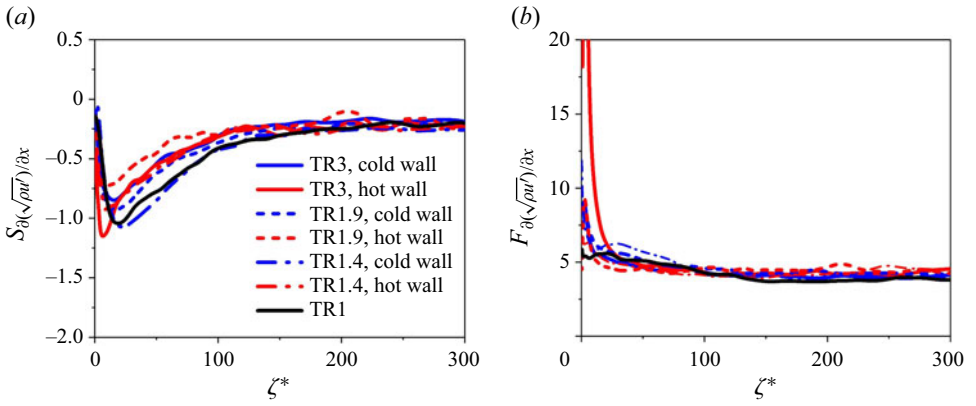

Figure 23. Moments of density-weighted velocity gradients $\partial(\sqrt{\rho}u')/\partial x$ in all cases: (*a*) S of $\partial(\sqrt{\rho}u')/\partial x$, (*b*) F of $\partial(\sqrt{\rho}u')/\partial x$.

Appendix C. Moments of density-weighted velocity gradients

Results of fluctuating velocity gradient shown in figure 6 are based on Reynolds-averaged velocity fluctuations, which are typically encountered in the past studies on incompressible turbulence (Kim & Antonia, 1993; Sreenivasan & Antonia, 1997; Schumacher *et al.* 2014; Antonia *et al.* 2015; Djenidi *et al*. 2017). In figure 23, we assess the skewness and flatness of derivatives of density-weighted velocity fluctuations $\sqrt{\rho}u'$ ($Z = \partial(\sqrt{\rho}u')/\partial x$ in (3.6)) taking account of the influences of density variations on fluctuating velocity (Patel *et al.* 2015; Hirai, Pecnik & Kawai 2021). The results show that the behaviours of the moments of $\partial(\sqrt{\rho}u')/\partial x$ agree with our previous results based on Reynolds-averaged velocity fluctuations. The comparisons of $S_{\partial(\sqrt{\rho}u')/\partial x}$ and $F_{\partial(\sqrt{\rho}u')/\partial x}$ for all channel flow cases also show a good collapse in the LIR, suggesting that employing density-weighted velocity fluctuations does not affect the validity of the conclusions; the plateau of $S_{\partial(\sqrt{\rho}u')/\partial x}$ and $F_{\partial(\sqrt{\rho}u')/\partial x}$ occurs in the LIR with $S_{\partial(\sqrt{\rho}u')/\partial x} = -0.25$ and $F_{\partial(\sqrt{\rho}u')/\partial x} = 4$, which bears striking analogies with the Reynolds-averaged results. Compared with the results in figure 5(*a*,*b*), the collapse in the LIR for $S_{\partial(\sqrt{\rho}u')/\partial x}$ and $F_{\partial(\sqrt{\rho}u')/\partial x}$ becomes more prominent because the effects of density variations on the statistics are partially eliminated.

References

Abe, H., Antonia, R. & Kawamura, H. 2009 Correlation between small-scale velocity and scalar fluctuations in a turbulent channel flow. *J. Fluid Mech.* **627**, 1–32.

Antonia, R.A., Djenidi, L., Danaila, L. & Tang, S.L. 2017 Small scale turbulence and the finite Reynolds number effect. *Phys. Fluids* **29**, 020715.

Antonia, R.A., Kim, J. & Browne, L.W.B. 1991 Some characteristics of small-scale turbulence in a turbulent duct flow. *J. Fluid Mech.* **233**, 369–388.

Antonia, R.A., Tang, S.L., Djenidi, L. & Danaila, L. 2015 Boundedness of the velocity gradient skewness in various turbulent flows. *J. Fluid Mech.* **781**, 727–744.

Belin, F., Maurer, P.T. & Willaime, H. 1997 Velocity gradient distributions in fully developed turbulence: an experimental study. *Phys. Fluids* **9**, 3843–3850.

Benzi, R., Ciliberto, S., Tripiccione, R., Baudet, C., Massaioli, F. & Succi, S. 1993 Extended self-similarity in turbulent flows. *Phys. Rev.* E **48**, 29–32.

Bolmatov, D., Brazhkin, V. & Trachenko, K. 2013 Thermodynamic behavior of supercritical matter. *Nat. Commun.* **4**, 2331.

Boschung, J., Hennig, F., Gauding, M., Pitsch, H. & Peters, N. 2016 Generalized higher-order Kolmogorov scales. *J. Fluid Mech.* **794**, 233–251.

Bradshaw, P. 1977 Compressible turbulent shear layers. *Annu. Rev. Fluid Mech.* **9**, 33–52.

CHUNG, T.H., AJLAN, M., LEE, L.L. & STARLING, K.E. 1988 Generalized multiparameter correlation for nonpolar and polar fluid transport properties. *Ind. Engng Chem. Res.* **27**, 671–679.

CHUNG, W.T., JUNG, K.S., CHEN, J.H. & IHME, M. 2022 BLASTNet: a call for community-involved big data in combustion machine learning. *Appl. Energy Combust. Sci.* **12**, 100087.

COLEMAN, G.N., KIM, J. & MOSER, R.D. 1995 A numerical study of turbulent supersonic isothermal-wall channel flow. *J. Fluid Mech.* **305**, 159–183.

CONGIUNTI, A., BRUNO, C. & GIACOMAZZI, E. 2003 Supercritical combustion properties. *AIAA Paper* 2003-478.

DJENIDI, L., ANTONIA, R., TALLURU, M. & ABE, H. 2017 Skewness and flatness factors of the longitudinal velocity gradient in wall-bounded flows. *Phys. Rev. Fluids* **2**, 064608.

DUAN, L., BEEKMAN, I. & MARTIN, M.P. 2011 Direct numerical simulation of hypersonic turbulent boundary layers. Part 3. Effect of Mach number. *J. Fluid Mech.* **672**, 245–267.

ELSING, G.E. & MARUSIC, I. 2010 Universal aspects of small-scale motions in turbulence. *J. Fluid Mech.* **662**, 514–539.

GARCIA, C.M., JACKSON, P.R. & GARCIA, M.H. 2005 Confidence intervals in the determination of turbulence parameters. *Exp. Fluids* **40**, 514–522.

GUO, J., YANG, X.I.A. & IHME, M. 2022 Structure of the thermal boundary layer in turbulent channel flows at transcritical conditions. *J. Fluid Mech.* **934**, A45.

HAMLINGTON, P.E., KRASNOV, D., BOECK, T. & SCHUMACHER, J. 2012 Local dissipation scales and energy dissipation-rate moments in channel flow. *J. Fluid Mech.* **701**, 419–429.

HICKEY, J.-P., MA, P.C., IHME, M. & THAKUR, S. 2013 Large eddy simulation of shear coaxial rocket injector: real fluid effects. *AIAA Paper* 2013-4071.

HIRAI, R., PECNIK, R. & KAWAI, S. 2021 Effects of the semi-local Reynolds number in scaling turbulent statistics for wall heated/cooled supersonic turbulent boundary layers. *Phys. Rev. Fluids* **6**, 124603.

HUANG, P.G., COLEMAN, G.N. & BRADSHAW, P. 1995 Compressible turbulent channel flows: DNS results and modelling. *J. Fluid Mech.* **305**, 185–221.

JIANG, H.Y., HU, X.Y., CHENG, L. & ZHOU, T.M. 2022 Direct numerical simulation of the turbulent kinetic energy and energy dissipation rate in a cylinder wake. *J. Fluid Mech.* **946**, A11.

KAWAI, S. 2019 Heated transcritical and unheated non-transcritical turbulent boundary layers at supercritical pressures. *J. Fluid Mech.* **865**, 563–601.

KERR, R.M. 1985 Higher-order derivative correlations and the alignment of small-scale structures in isotropic numerical turbulence. *J. Fluid Mech.* **153**, 31–58.

KIM, J. & ANTONIA, R.A. 1993 Isotropy of the small scales of turbulence at low Reynolds number. *J. Fluid Mech.* **251**, 219–238.

KIM, K., HICKEY, J.-P. & SCALO, C. 2019 Pseudophase change effects in turbulent channel flow under transcritical temperature conditions. *J. Fluid Mech.* **871**, 52–91.

KOLMOGOROV, A.N. 1941 The local structure of turbulence in incompressible fluid for very large Reynolds number. *Dokl. Akad. Nauk SSSR* **30**, 299–303.

KOLMOGOROV, A.N. 1962 A refinement of previous hypotheses concerning the local structure of turbulence in a viscous incompressible fluid at high Reynolds number. *J. Fluid Mech.* **13**, 82–85.

LEPORE, J. & MYDLARSKI, L. 2012 Finite-Peclet-number effects on the scaling exponents of high-order passive scalar structure functions. *J. Fluid Mech.* **713**, 453–481.

LI, F.B., GUO, J., BAI, B.F. & IHME, M. 2023 Analysis of real-fluid thermodynamic effects on turbulent statistics in transcritical channel flows. *Phys. Rev. Fluids* **8**, 024605.

LUMLEY, J.L. & NEWMAN, G.R. 1977 The return to isotropy of homogeneous turbulence. *J. Fluid Mech.* **82**, 161–178.

MA, P.C., YANG, X.I.A. & IHME, M. 2018 Structure of wall-bounded flows at transcritical conditions. *Phys. Rev. Fluids* **3**, 034609.

MESTAYER, P. 1982 Local isotropy and anisotropy in a high-Reynolds-number turbulent boundary layer. *J. Fluid Mech.* **125**, 475–503.

MILLER, R.S., HARSTAD, K.G. & BELLAN, J. 2001 Direct numerical simulations of supercritical fluid mixing layers applied to heptane–nitrogen. *J. Fluid Mech.* **436**, 1–39.

OBUKHOV, A.M. 1962 Some specific features of atmospherical turbulence. *J. Fluid Mech.* **125**, 475–503.

PATEL, A., PEETERS, J.W.R., BOERSMA, B.J. & PECNIK, R. 2015 Semi-local scaling and turbulence modulation in variable property turbulent channel flows. *Phys. Fluids* **27**, 095101.

PENG, D.-Y. & ROBINSON, D. B. 1976 A new two-constant equation of state. *Ind. Engng Chem. Fundam.* **15**, 59–64.

POLING, B.E., PRAUSNITZ, J.M. & O'CONNELL, J.P. 2001 *The Properties of Gases and Liquids*. McGraw-Hill.

POPE, S. 2000 *Turbulent Flows*. Cambridge University Press.
PUMIR, A., XU, H.T. & SIGGIA, E.D. 2016 Small-scale anisotropy in turbulent boundary layers. *J. Fluid Mech.* **804**, 5–23.
SCHUMACHER, J. 2001 Derivative moments in stationary homogeneous shear turbulence. *J. Fluid Mech.* **441**, 109–118.
SCHUMACHER, J. 2007 Sub-Kolmogorov scale fluctuations in fluid turbulence. *Europhys. Lett.* **80**, 54001.
SCHUMACHER, J., SCHEEL, J.D., KRASNOV, D., DONZIS, D.A., YAKHOT, V. & SREENIVASAN, K.R. 2014 Small-scale universality in fluid turbulence. *Proc. Natl Acad. Sci. USA* **111**, 10961–10965.
SCIACOVELLI, L., CINNELLA, P. & GRASSO, F. 2017 Small-scale dynamics of dense gas compressible homogeneous isotropic turbulence. *J. Fluid Mech.* **825**, 515–549.
SENGUPTA, U., NEMATI, H., BOERSMA, B.J. & PECNIK, R. 2017 Fully compressible low-Mach number simulations of carbon-dioxide at supercritical pressures and trans-critical temperatures. *Flow Turbul. Combust.* **99** (3–4), 909–931.
SHE, Z.S. & LEVEQUE, E. 1994 Universal scaling laws in fully developed turbulence. *Phys. Rev. Lett.* **72** (3), 336–339.
SIMEONI, G., BRYK, T., GORELLI, F., KRISCH, M., RUOCCO, G., SANTORO, M. & SCOPIGNO, T. 2010 The widom line as the crossover between liquid-like and gas-like behaviour in supercritical fluids. *Nat. Phys.* **6**, 503–507.
SIMESKI, F. & IHME, M. 2023 Supercritical fluids behave as complex networks. *Nat. Commun.* **14**, 1996.
SREENIVASAN, K. R. & ANTONIA, R. A. 1997 The phenomenology of small-scale turbulence. *Annu. Rev. Fluid Mech.* **29**, 435–472.
TANG, S., ANTONIA, L., A, R., DJENIDI, L., ABE, H., ZHOU, T., DANAILA, L. & ZHOU, Y. 2015 Transport equation for the mean turbulent energy dissipation rate on the centerline of a fully developed channel flow. *J. Fluid Mech.* **777**, 151–177.
TANG, S.L., ANTONIA, R.A., DJENIDI, L. & ZHOU, Y. 2019 Can small-scale turbulence approach a quasi-universal state. *Phys. Rev. Fluids* **4**, 024607.
TAYLOR, G.I. 1935 Statistical theory of turbulence. *Proc. R. Soc. Lond.* A*: Math. Phys. Engng Sci.* **151**, 421–444.
TOKI, T., TERAMOTO, S. & OKAMOTO, K. 2020 Velocity and temperature profiles in turbulent channel flow at supercritical pressure. *J. Propul. Power* **36**, 3–13.
VAN ATTA, C.W. & ANTONIA, R.A. 1980 Reynolds number dependence of skewness and flatness factors of turbulent velocity gradients. *Phys. Fluids* **23**, 252–257.
VREMAN, A.W. & KUERTEN, J.G.M. 2014 Comparison of direct numerical simulation databases of turbulent channel flow. *Phys. Fluids* **26**, 015102.
VAN DE WATER, W. & HERWEIJER, J.A. 1999 High-order structure functions of turbulence. *J. Fluid Mech.* **387**, 3–37.
XU, G., ANTONIA, R.A. & RAJAGOPALAN, S. 2001 Sweeping decorrelation hypothesis in a turbulent round jet. *Fluid Dyn. Res.* **28**, 311–321.
YAKHOT, V. 2006 Probabilities in strong turbulence. *Physica* D **215**, 166–174.
YAKHOT, V. & SREENIVASAN, K.R. 2005 Anomalous scaling of structure functions and dynamic constraints on turbulence simulations. *J. Stat. Phys.* **121**, 823–884.
ZHANG, P.J.Y., WAN, Z.H., LIU, N.S., SUN, D.J. & LU, X.Y. 2022 Wall-cooling effects on pressure fluctuations in compressible turbulent boundary layers from subsonic to hypersonic regimes. *J. Fluid Mech.* **946**, A14.
ZHANG, Y.S., BI, W.T., HUSSAIN, S., LI, X.L. & SHE, Z.S. 2012 Mach-number-invariant mean-velocity profile of compressible turbulent boundary layers. *Phys. Rev. Lett.* **109**, 054502.